1 **Title: Starvation induces shrinkage of the bacterial cytoplasm**

2

3 **Authors:** Handuo Shi[1,2,†], Corey S. Westfall[3,†], Jesse Kao[3], Pascal D. Odermatt[1,4], Spencer

4 Cesar[4], Montana Sievert[3], Jeremy Moore[3], Carlos G. Gonzalez[5], Lichao Zhang[6], Joshua E.

5 Elias[6], Fred Chang[4], Kerwyn Casey Huang[1,2,6,*], Petra Anne Levin[3,*]

6

7 [1]Department of Bioengineering, Stanford University, Stanford, CA 94305

8 [2]Department of Microbiology and Immunology, Stanford University School of

9 Medicine, Stanford, CA 94305

10 [3]Department of Biology, Washington University in St. Louis, St. Louis, MO 63130

11 [4]Department of Cell and Tissue Biology, University of California, San Francisco, San

12 Francisco, CA 94143

13 [5]Department of Chemical and Systems Biology, Stanford University School of Medicine,

14 Stanford, CA 94305

15 [6]Chan Zuckerberg Biohub, San Francisco, CA 94158

16

17 [†]: These authors contributed equally to this study

18 [*]: Correspondence: kchuang@stanford.edu and plevin@wustl.edu

19

20 Keywords: *stationary phase; starvation; MlaA; turgor pressure; periplasm; osmolarity Tol-Pal*

Abstract

Environmental fluctuations are a common challenge for single-celled organisms; enteric bacteria such as *Escherichia coli* experience dramatic changes in nutrient availability, pH, and temperature during their journey into and out of the host. While the effects of altered nutrient availability on gene expression and protein synthesis are well known, their impacts on cytoplasmic dynamics and cell morphology have been largely overlooked. Here, we discover that depletion of utilizable nutrients results in shrinkage of *E. coli's* inner membrane from the cell wall. Shrinkage was accompanied by a ~17% reduction in cytoplasmic volume and a concurrent increase in periplasmic volume. Inner membrane retraction occurred almost exclusively at the new cell pole. This phenomenon was distinct from turgor-mediated plasmolysis and independent of new transcription, translation, or canonical starvation-sensing pathways. Cytoplasmic dry-mass density increased during shrinkage, suggesting that it is driven primarily by loss of water. Shrinkage was reversible: upon a shift to nutrient-rich medium, expansion started almost immediately at a rate dependent on carbon-source quality. Robust recovery from starvation required the Tol-Pal system, highlighting the importance of envelope coupling during recovery. *Klebsiella pneumoniae* also exhibited shrinkage when shifted to carbon-free conditions, suggesting a conserved phenomenon. These findings

40 demonstrate that even when Gram-negative bacterial growth is arrested, cell

41 morphology and physiology are still dynamic.

42 **Significance statement**

43 Bacterial cells constantly face nutrient fluctuations in their natural environments. While
44 previous studies have identified gene expression changes upon nutrient depletion, it is
45 much less well known how cellular morphology and cytoplasmic properties respond to
46 shifts in nutrient availability. Here, we discovered that switching fast-growing
47 *Escherichia coli* cells to nutrient-free conditions results in substantial shrinkage of the
48 inner membrane away from the cell wall, especially at the new pole. Shrinkage was
49 primarily driven by loss of cytoplasmic water contents. Shrinkage was also exhibited by
50 cells naturally entering stationary phase, highlighting its biological relevance across
51 starvation conditions. The membrane-spanning Tol-Pal system was critical for robust
52 entry into and recovery from shrinkage, indicating the importance of cell-envelope
53 homeostasis in surviving nutrient starvation.

54 **Introduction**

55

56 As single-celled organisms, bacteria are frequently at the mercy of their environment,
57 with the cell envelope serving as the front line of defense. Shifts in temperature, ionic
58 concentration, and nutrient availability result in changes in cell shape and morphology
59 through their impacts on lipid and cell-wall synthesis and cell-cycle progression (1).
60 Decades of work on the many ways bacteria adapt to changing environmental
61 conditions have provided insights into transcriptional (2) and post-transcriptional (3)
62 responses to environmental changes. Less clear is the impact of rapid changes in the
63 environment, particularly nutrient depletion, on cell shape and physiology.

64

65 Like many gut commensals and pathogens, the model organism *Escherichia coli*
66 experiences a dramatic change in nutrient abundance as it travels through the rich host
67 gut into the comparatively dilute environment. Gradual depletion of nutrients is
68 associated with exit from exponential growth and entry into the relatively quiescent
69 state known as stationary phase (4). More rapid depletion of carbon or nitrogen leads to
70 the starvation stringent response characterized by accumulation of the small molecules
71 guanosine penta- and tetraphosphate (abbreviated here as ppGpp). ppGpp down
72 regulates biosynthesis, driving exit from exponential growth, reducing metabolic
73 activity, and eventually stimulating entry into stationary phase. Both entry into

74 stationary phase and ppGpp accumulation have global effects on gene expression and
75 cellular composition (5), alter the structure of the cell envelope (4), and increase
76 resistance to diverse stresses (6).
77
78 To explore the physical effects of carbon starvation, we examined the effects of sudden
79 removal of carbon from exponentially growing *E. coli* cells. We found that shifting from
80 nutrient-replete to nutrient-deficient medium led to rapid growth arrest and shrinkage
81 of the cytoplasm at the new pole in a manner distinct from osmotic shock-induced
82 plasmolysis. We determined that shrinkage is coupled to densification of the cytoplasm
83 and decreased abundance of translation-related proteins; shrinkage was not affected by
84 a wide range of genetic or chemical perturbations. Cytoplasmic shrinkage also occurred
85 during entry into stationary phase, suggesting that the root cause of shrinkage is
86 nutrient depletion and/or an inability to access available nutrients. The rate of recovery
87 from starvation-induced shrinkage was dependent on the quality of the re-supplied
88 carbon source, and robust recovery required the Tol-Pal system, which is important for
89 maintaining outer-membrane integrity. Other Gram-negative species also exhibited
90 cytoplasmic shrinkage, suggesting that this phenomenon is a general adaptation to
91 starvation independent of previously characterized regulatory mechanisms.

92 **Results**

93

94 ***Transition from exponential growth to carbon-free medium induces cytoplasmic***

95 ***shrinkage***

96 To test the physiological effects of sudden carbon removal, we first cultured wild-type *E.*

97 *coli* MG1655 cells to mid-exponential phase in LB and minimal M9 medium

98 supplemented with 0.4% glucose (Methods). Cells sampled from each condition were

99 washed three times in M9 salts (M9 without added carbon), resuspended in M9 salts,

100 spotted on agarose pads containing M9 salts, and imaged via phase-contrast

101 microscopy (Methods, Fig. 1A). Within the time required to wash and resuspend the

102 cells and mount them on a slide (~10 min), a readily visible phase-light region appeared

103 at the pole of nearly every cell regardless of initial culture condition (Fig. 1B, left). In

104 contrast to the short, stubby morphology adopted by stationary-phase *E. coli* cells (7) or

105 in response to ppGpp accumulation (8), cells retained a rod-like shape after sudden

106 carbon starvation (Fig. 1B, left). Importantly, resuspending cells in their original

107 medium did not result in formation of the phase-light region (Fig. 1B, right), indicating

108 that this phenomenon is a consequence of sudden carbon depletion. Shrinkage was not

109 specific to M9 salts; similar behavior was observed transitioning from AB minimal

110 salts+0.2% glucose to AB salts alone (Fig. S1A). The Gram-negative species *Klebsiella*

111 *pneumoniae* also exhibited shrinkage after abrupt starvation, indicating that the

112 phenomenon is not limited to *E. coli* (Fig. 1C). Resuspension of *E. coli* MG1655 cells
113 cultured in M9 salts+0.4% glucose in nitrogen-free (lacking NH_4Cl) M9+glucose
114 similarly resulted in formation of a phase-light pole, albeit on a longer time scale (Fig.
115 S1B), suggesting the phenomenon is generally associated with sudden depletion of
116 nutrients.
117
118 The phase-light area at cell poles corresponded to an enlargement of the periplasm, the
119 compartment between *E. coli's* inner and outer membrane. To clarify the nature of the
120 starvation-induced change in cell morphology, we stained MG1655 cells switched from
121 LB to M9 salts with FM4-64 and MitoTracker, which preferentially stain the outer and
122 inner membranes, respectively (9). Carbon starvation led to clear separation between
123 the FM4-64 and MitoTracker contours at one end of the cell, consistent with an enlarged
124 periplasm (Fig. 1D). We segmented the FM4-64 and MitoTracker cell contours
125 (Methods) for log-phase and starved cells and found that starvation resulted in a ~17%
126 mean decrease in cytoplasmic volume (Fig. 1E).
127
128 While cytoplasmic condensation and the formation of gaps between the outer and inner
129 membranes (plasmolysis) are characteristic of hyperosmotic shock, starvation-induced
130 inner membrane retraction appears to be a separate phenomenon. Classically,
131 hyperosmotic shock causes plasmolysis when the increase in external osmotic pressure

132 is ~100 mM (10). We measured the osmolality of LB medium to be 252 mOsm/L, and M9
133 salts have an osmolality of 250 mOsm/L (11). Therefore, switching from LB to M9 salts
134 largely maintained the external osmotic pressure, and the switch from M9 glucose to
135 M9 salts actually decreased the external osmotic pressure by ~22 mM due to the
136 removal of glucose. Hence, a switch to M9 salts does not induce hyperosmotic shock
137 (12). Moreover, close examination of starved and hyperosmotic-shocked cells revealed
138 distinct differences between the two conditions with regard to cell envelope and
139 cytoplasmic morphology (Fig. 1F). To directly compare starvation-induced shrinkage
140 with the effects of hyperosmotic shock, we placed MG1655 cells growing exponentially
141 in LB on pads with LB+20% sucrose along with the inner-membrane stain MitoTracker
142 (Methods); 20% sucrose induces an osmotic shock of ~0.6 M. The phase-contrast and
143 MitoTracker signals showed multiple plasmolysis bays along the body of most cells,
144 unlike starvation-induced shrinkage (Fig. 1F,G). More than 70% of hyperosmotic-
145 shocked cells exhibited plasmolysis at both poles, while starvation-induced shrinkage
146 occurred predominantly at one pole (Fig. 1F,H). Thus, starvation-induced shrinkage is
147 unlikely to be due to acute changes in the osmotic balance across the cell envelope.
148

149 ***Shrinkage increases gradually with the extent and duration of nutrient removal***

150 To better quantify periplasmic and cytoplasmic areas under various nutrient conditions,
151 we constructed an MG1655 strain (KC1193) that expresses cytoplasmic GFP

152 constitutively and periplasmic mCherry from the lactose promoter (Methods). We
153 transitioned KC1193 cells from M9 salts+0.4% glucose to M9 without carbon via three
154 washes as above, and then incubated the resuspended pellet for 4 h before imaging (Fig.
155 1A). Periplasmic mCherry accumulated at one pole of the overwhelming majority of
156 cells (105/121 cells, Fig. 2A), consistent with shrinkage of the cytoplasm away from the
157 outer membrane, unlike log-phase cells in which the mCherry signal was uniform along
158 the cell periphery.
159
160 To determine whether shrinkage required complete removal of nutrients, we imaged
161 KC1193 cells after 4 h of incubation after 0, 1, 2, or 3 washes in M9. Shrinkage increased
162 after each of the first two washes, and then plateaued at ~17% (Fig. 2B). Thus, residual
163 nutrients are sufficient to inhibit shrinkage. To track the dynamics of shrinkage, we
164 used a microfluidic flow cell to image KC1193 cells throughout the switch from LB to
165 M9 salts without carbon (Fig. 2C). The cytoplasm started to shrink after <10 min and
166 continued to shrink for ~2 h (Fig. 2D). Similar qualitative dynamics were observed for
167 cells switched from M9+0.4% glucose to M9 salts. After normalizing for cell volume, the
168 rate of shrinkage was faster for cells transitioning from LB compared with M9+glucose
169 (Fig. 2D), suggesting shrinkage may reflect a lag between nutrient depletion and the
170 subsequent downregulation of biosynthetic capacity. Thus, shrinkage is a gradual
171 process that starts soon after starvation and extends over hours, indicating a process

172 highly distinct from the rapid, physical response to osmotic shock.

173

174 ***Shrinkage occurs at the new cell pole***

175 At each cell division, the mother cell creates daughter cells, with one new pole
176 representing the site of division. Given the distinctly polar nature of cytoplasmic
177 shrinkage following sudden starvation, we wondered if shrinkage might occur more
178 frequently at either the old or new pole. To assess this possibility, we added Alexa488-
179 wheat germ agglutinin (WGA) to wild-type MG1655 cells during growth (Methods) to
180 uniformly label the cell surface (13). We then washed out the fluorescent WGA and
181 grew the cells for approximately one cell doubling, so that the new pole would be dark
182 while old poles remained labeled due to their relative lack of growth. We switched cells
183 from LB to M9 salts for 4 h to induce cytoplasmic shrinkage. From a comparison of
184 phase-contrast and WGA fluorescence images, shrinkage clearly occurred at the new
185 (unlabeled) pole in the vast majority of cells (>90%) (Fig. 2E), suggesting that
186 attachment between the inner membrane and cell wall/outer membrane is weaker at the
187 new pole than at the old pole.

188

189 ***Starvation-induced cytoplasmic shrinkage is characterized by increased cell density***

190 To determine whether cells lose material during shrinkage, we assessed dry-mass cell
191 density before and after shrinkage via quantitative phase imaging, which uses *z*-stacks

192 of brightfield images to compute density-dependent phase shifts (14-18). Consistent
193 with previous reports (14, 15), dry-mass density in the cytoplasm was ~80% higher in
194 stationary phase than in log phase (Fig. 2F). Highlighting that the shrunken state is
195 distinct from stationary phase, the dry-mass density of suddenly starved cells
196 (transitioned from LB to M9 salts for 4 h) was intermediate between the densities of
197 stationary- and log-phase cells (Fig. 2F). Importantly, the density increase in starved
198 cells relative to log-phase cells was ~25%. Considering that the cytoplasmic volume
199 shrunk by ~17%, the density increase largely offsets the decrease in cytoplasmic volume
200 and maintains total cell dry mass (relative mass of the shrunken cells = (1+0.25)×(1-0.17)
201 = 1.04). Indeed, the distribution of total dry mass per cell was highly similar between
202 log-phase and starved cells (Fig. 2G). The periplasmic region remained at a dry-mass
203 density close to zero. Thus, these results suggest that cells shrink by losing water while
204 retaining most of their cytoplasmic contents.
205
206 ***Shrinkage is not coupled to a change in cytoplasmic diffusion***
207 Based on increases in cytoplasmic density (Fig. 2F), we wondered whether diffusion
208 was limited in starved cells. Reduced rates of cytoplasmic diffusion have been
209 observed in *E. coli* cells after hyperosmotic shock-induced plasmolysis (19) and
210 treatment with 2,4-dinitrophenol (DNP) (20), an oxidative phosphorylation uncoupler
211 that depletes cells of ATP energy. To assess cytoplasmic properties after sudden

212 nutrient depletion, we measured the diffusion constant of a GFP-labeled self-
213 assembling viral protein μNS (20). The larger size of the assembled μNS particles
214 results in slower diffusion than single proteins, making their motion easier to track than
215 the motion of individual GFP molecules. We fit the slope of mean-squared displacement
216 over time to extract a diffusion constant along the length dimension defined by the cell
217 midline (Fig. S2A, Methods), and our measured diffusion constants for exponentially-
218 growing cells were consistent with previous results (20). Somewhat surprisingly, while
219 DNP treatment reduced diffusion as expected (20), the diffusion constant was
220 essentially equivalent in exponentially growing cells and in starved, shrunken cells (Fig.
221 S2B). These findings indicate that the increase in cytoplasmic density during acute
222 carbon starvation is insufficient to alter the diffusive motion of these nanoparticles, and
223 suggest that the impact of starvation on metabolic activity is distinct to that of DNP
224 treatment.
225
226 ***Shrinkage is independent of biosynthesis, stress-response pathways, and regulatory***
227 ***circuits governing cell-envelope homeostasis***
228 Precisely orchestrated changes in transcription, translation, and/or proteolysis are
229 characteristic of diverse bacterial stress-response pathways. Inhibiting any one of these
230 major biosynthetic processes typically interferes with the ability of cells to adapt to new
231 conditions. To determine whether new biosynthesis is required for cytoplasmic

232 shrinkage, we added the following antibiotics to M9 salts during the initial washes and
233 during resuspension: rifampicin, to inhibit transcription; chloramphenicol, to inhibit
234 translation; cerulenin, to inhibit lipid synthesis; and A22, to inhibit cell-wall synthesis.
235 In all cases, shrinkage still occurred, indicating that the phenomenon is independent of
236 major biosynthetic pathways (Fig. S2C).
237
238 Next, we sought to determine the effect of previously characterized stress-response
239 pathways associated with nutrient limitation on shrinkage. In *E. coli*, depletion of
240 carbon and/or nitrogen induces accumulation of ppGpp, resulting in down-regulation
241 of a wide range of biosynthetic pathways and a concomitant reduction in growth (21,
242 22). The transcriptional regulator RpoS (SigmaS), which is induced in response to
243 diverse stresses (23, 24), is also important for entry into stationary phase, a state
244 associated with nutrient depletion as well as cell crowding. Surprisingly given the
245 central roles of RpoS and ppGpp in starvation-induced stress responses, cells defective
246 in RpoS (Δ*rpoS*) or ppGpp synthesis and accumulation (Δ*relA* Δ*spoT*) exhibited
247 cytoplasmic shrinkage after washing and incubation in M9 salts (Fig. S2D). Δ*rpoS* cells
248 were phenotypically indistinguishable from wild-type cells in this regard. Populations
249 of ppGpp mutants are notoriously heterogeneous in size, with ~10% of cells forming
250 long aseptate filaments (25). Nevertheless, periplasmic expansion was readily visible at
251 the poles of Δ*relA* Δ*spoT* cells regardless of the degree of filamentation (Figure S2D),

252 indicating that shrinkage was independent of ppGpp production. Shrinkage also
253 occurred in cells lacking ClpP (Figure S2D), a serine protease required for adaptation to
254 and extended viability in stationary phase (26, 27). Thus, as with the chemical inhibitors
255 of biosynthesis described above, the degree and frequency of shrinkage was
256 independent of all of these stress-response pathways.
257
258 Starvation-induced shrinkage also occurred in cells defective in carbon acquisition and
259 metabolism. Deletion of the gene encoding Crr, a phosphotransfer protein involved in
260 the uptake and phosphorylation of glucose and several other carbon sources (28), or
261 Pgi, which catalyzes the interconversion of glucose-6-phosphate and fructose-6-
262 phosphate during glycolysis and gluconeogenesis (29), had no impact on the timing or
263 extent of cytoplasmic shrinkage (Fig. S2D). Finally, despite a superficial similarity
264 between shrunken cells and cells defective in outer membrane lipid homeostasis (7),
265 deletion of MlaA, a lipoprotein involved in maintenance of outer-membrane lipid
266 asymmetry through retrograde phospholipid trafficking (30), did not affect the
267 frequency or degree of shrinkage (Fig. S2D). Thus, shrinkage does not require
268 biosynthesis, induction of known stress-response pathways, or regulation of cell-
269 envelope homeostasis.
270
271 ***Proteins involved in translation and DNA replication are down-regulated during***

272 ***starvation***

273 To determine if starvation-induced shrinkage is associated with distinct shifts in
274 proteome composition, we extracted proteins from log-phase cells and cells acutely
275 starved for 4 h, and analyzed protein abundances using mass spectrometry (Methods,
276 Table S1). No protein classes exhibited a significantly higher protein abundance in
277 starved cells versus log-phase cells, and the only gene classes with a significant decrease
278 in starved cells involved translation or DNA replication (Fig. 2H); for the latter, the
279 slight ~5% average decrease was predominantly due to lower levels of five proteins (Fig.
280 2H). Thus, only the machinery responsible for rapid growth is affected by acute
281 starvation.

282

283 ***The rate of cytoplasmic recovery depends on the quality of carbon source***

284 Importantly, shrinkage is reversible in wild type cells. Plating wild-type MG1655 and
285 BW25113 cells 4 h after a shift from LB to M9 salts resulted in ~100% recovery (Fig. 3A).
286 The viability of shrunken cells was confirmed by staining them with propidium iodide
287 (Fig. 3B), a DNA intercalator that only enters cells with compromised plasma
288 membranes and as such is frequently used as a live/dead indicator (31).

289

290 To determine the dynamics of recovery, we placed cells starved in M9 salts onto an
291 M9+0.4% glucose agarose pad with MitoTracker stain and monitored regrowth using

292 time-lapse microscopy (Methods). The cytoplasm began to re-expand almost
293 immediately after the cells were placed on the agarose pad (Fig. 3C), indicating that the
294 cells were ready to regrow despite prolonged starvation. Notably, starved cells
295 exhibited bright foci of MitoTracker signal at the boundary of the cytoplasm (Fig. 3C,
296 white arrows); such foci are indicative of folded membrane (32) and suggest that
297 shrinkage is not due to cells metabolizing membrane components and thereby
298 compressing the cytoplasm. In support of this interpretation, the maximum
299 MitoTracker signal after normalization was significantly higher in starved cells than in
300 log-phase cells (Fig. 3D). Plasma-membrane foci dissolved as the cytoplasm re-
301 expanded, with complete dissolution coinciding with the cytoplasm rejoining the cell
302 wall (Fig. 3C).
303
304 We further quantified the rate of normalized area expansion during recovery.
305 Expansion was initially relatively fast (0.007 min^{-1}), but once the cytoplasm reached the
306 size of the cell envelope, expansion slowed down to <0.002 min^{-1} (corresponding to a
307 doubling time of >5 h, Fig. 3E). We term these two expansion phases as the "recovery"
308 and "growth" phases, respectively. Even during the faster recovery phase, the rate of
309 expansion was slower than the growth rate of exponentially growing cells in M9+0.4%
310 glucose (~0.01 min^{-1}), consistent with a reduction in translational machinery (Fig. 2H).
311 The rapid slowdown in growth once the cytoplasm reached the size of the rest of the

312 cell envelope (Fig. 3E) suggests that the cell wall either mechanically resisted expansion
313 or that growth of the cell envelope was slower than cytoplasmic growth during the
314 period over which the cells were tracked.
315
316 To determine whether recovery was dependent on the presence of a metabolizable
317 carbon source, we examined the behavior of starved cells on M9 agarose pads
318 supplemented with a variety of carbon sources. The initial recovery rate was slower on
319 carbon sources that support slower steady-state growth rates (Fig. 3F). Importantly,
320 addition of 3-O-methyl-glucose, which is imported and phosphorylated rather than
321 metabolized (33), did not stimulate recovery (Fig. 3F), indicating that recovery requires
322 synthesis. These data, along with the observation that the first recovery phase requires
323 tens of minutes (Fig. 3E) rather than the seconds required to swell a cell after
324 hypoosmotic shock (10), indicate that metabolism drives recovery.
325
326 To probe potential drivers of recovery after cytoplasmic shrinkage, we examined the
327 impact of antibiotic treatment on recovery. Cytoplasmic re-expansion was observed in
328 the presence of rifampicin, chloramphenicol, cerulenin, and A22, although all four
329 compounds slowed down recovery and outgrowth (Fig. 3G,H). Together, these data
330 suggest that while re-expansion relies on active metabolism of fresh nutrients, it does
331 not directly depend on new transcription, translation, or envelope synthesis.

332

333 ***Analysis of stationary-phase cells suggests that shrinkage is a general response to***

334 ***depletion of useful nutrients***

335 To determine whether cytoplasmic shrinkage constitutes a more general response to

336 nutrient depletion beyond abrupt starvation, we examined stationary-phase KC1193

337 cells after 18 h of growth in LB. In these cells, periplasmic mCherry was clearly

338 concentrated at one pole, signifying some degree of cytoplasmic shrinkage (Fig. 4A).

339 Surprisingly, shrinkage was visible in some cells in phase-contrast images (Fig. 4A,

340 white arrows), suggesting that it had been overlooked in previous studies of stationary-

341 phase cell morphology.

342

343 Resuspension of stationary-phase KC1193 cells in fresh LB resulted in resolution of

344 polar mCherry signal within ~150 min (Fig. 4A,B, S3A), a time frame similar to the

345 population based-lag time determined by optical density (Fig. 4B, inset). Mutants that

346 increased (e.g. Δ*rpoS*) or reduced (Δ*cyaA*) lag time resolved periplasmic area in a longer

347 and shorter time period, respectively (Fig. 4B, S3A), consistent with resolution reflecting

348 the ability of different strains to ramp up metabolism. Shrinkage was also observed in

349 KC1193 cells cultured overnight in LB supplemented with a range of glucose

350 concentrations from 0-2%: cells grown overnight in LB+0.2-0.3% glucose exhibited the

351 most obvious shrinkage, both in total periplasmic area (Fig. 4C) and relative to cell size

352 (Fig. 4D). Thus, shrinkage is a general, sometimes dramatic, feature of stationary-phase
353 as well as abruptly starved cells, and the extent of shrinkage varies across mutants and
354 nutrient conditions.
355
356 ***Shrinkage is directly connected with growth during starvation and recovery***
357 To assess the kinetics of shrinkage in relation to cell growth, we shifted log-phase
358 KC1193 cells from fresh LB to spent medium (filtered supernatant from an 18-h
359 stationary-phase culture) and back to fresh LB after 100 min in a microfluidic flow cell
360 (Fig. 5A, Methods). We employed spent LB rather than AB salts to ensure that
361 osmolarity remained constant throughout the experiment and to further interrogate the
362 nature of shrinkage during stationary phase. Growth was immediately curtailed
363 following a switch to spent LB and halted completely within 10 min (Fig. 5B). We
364 detected increases in periplasmic area only after growth completely ceased (Fig. 5B),
365 further supporting the conclusion that shrinkage only occurs in the absence of cell
366 growth. The addition of fresh LB at t=110 min resulted in an immediate increase in both
367 cytoplasmic volume and growth rate (Fig. 5B), suggesting that recovery from shrinkage
368 is connected with growth resumption under these conditions. As with recovery from
369 abrupt starvation, the gradual increase in growth rate is consistent with the decrease in
370 abundance of translation-related proteins during shrinkage (Fig. 2H).
371

372 ***A functional Tol-Pal system is required for shrinkage and recovery***

373 Although disruption of cell-wall synthesis during elongation via A22 treatment did not
374 alter shrinkage or recovery (Fig. 3G,H, S2C), the predominance of shrinkage at the new
375 pole (Fig. 2E) led us to hypothesize that disruption of cell division would alter
376 shrinkage or recovery. The Tol-Pal system plays a role in outer-membrane invagination
377 and septal peptidoglycan processing during cell division (34) and is important for
378 maintaining outer membrane integrity (35). Intriguingly, carbon-starved Δ*tolA* cells
379 exhibited diverse single-cell phenotypes (Fig. 6A): a small subpopulation exhibited
380 shrinkage like wild-type cells (36/209), while the majority of cells either lysed (62/209) or
381 developed membrane blebs at cell poles or mid-cell (78/209), and another
382 subpopulation exhibited chaining (16/209). Similar phenotypes were also observed for
383 other genetic deletions in the Tol-Pal pathway, including Δ*tolB*, Δ*tolR*, and Δ*pal* (Fig. S4).
384 All Tol-Pal pathway deletion mutants also exhibited 50-70% lower CFU yields after
385 starvation-induced shrinkage (Fig. 6B).

386

387 Since the shrinkage phenotype was also induced naturally in stationary-phase cells (Fig.
388 4A), we further investigated the Tol-Pal deletions in stationary phase. The
389 morphologies of stationary-phase Δ*tolA* cells were similar to wild type. However, when
390 Δ*tolA* cells were placed onto agarose pads containing fresh medium, only a fraction
391 resumed growth (unlike wild-type cells in which virtually all cells regrew): during a 3-h

392 time-lapse imaging of 271 Δ*tolA* cells, 47 cells exhibited no growth and eventually lysed,
393 29 cells first grew but then lysed before the first cell division, and only 195 cells
394 resumed growth normally (Fig. 6C). Similar trends were observed in other Tol-Pal
395 deletions (Fig. 6C). Taken together, these data suggest that coordination between the
396 inner and outer membranes is essential for efficient recovery from starvation.
397
398 To test the hypothesis that shrinkage results from a disruption of coordination between
399 the inner and outer membranes, we were motivated by previous studies showing that
400 treatment with globomycin, an inhibitor of outer membrane biogenesis through its
401 impact on activity of lipoprotein-specific signal peptidase II (LspA), induces
402 condensation of the bacterial chromosome (36). We tested the impact of 20 ug/mL
403 globomycin (~2X MIC) on the morphology of exponentially growing wild-type cells.
404 Globomycin treatment resulted in a phenotype nearly identical to that observed in
405 carbon-starved cells, with a reduction in cytoplasmic volume and enlargement of the
406 periplasm at a single pole (Fig. 6D), supporting disruption of inner and outer
407 membrane biogenesis as a driver of shrinkage.

408 **Discussion**

409

410 In this study, we determined that two types of starvation—sudden limitation of
411 nutrients and stationary phase—induces the *E. coli* cytoplasm to shrink away from the
412 cell wall and outer membrane (Fig. 1), increasing cytoplasmic density ~1.3-fold (Fig. 2F).
413 Our data suggest that homeostatic connections between inner and outer membrane
414 biogenesis play a role in both shrinkage and recovery. Treatment with globomycin, an
415 inhibitor of lipoprotein secretion and outer membrane biogenesis, induced shrinkage in
416 exponentially growing cells that was phenotypically indistinguishable from that caused
417 by sudden nutrient depletion (Fig. 6D). Consistent with the notion that defects in inner
418 and outer membrane coordination contribute to shrinkage, a gain-of-function mutation
419 in MlaA (*mlaA**), which contributes to retrograde phospholipid transport (30), leads to
420 cytoplasmic shrinkage when *E. coli* is resuspended in spent LB medium (7). The
421 lipoprotein MlaA removes phospholipids from the outer leaflet of the outer membrane
422 and shuttles them to the periplasm, making it important for outer membrane
423 asymmetry (30). Shrinkage in exponentially growing cells with altered phospholipid
424 synthesis (37) further indicates that dysbiosis between inner and outer membrane
425 biogenesis is a major contributor to shrinkage.

426

427 Recovery from cytoplasmic shrinkage appears to be similarly dependent on inner and

428 outer membrane coordination. Although they do not appear to impact shrinkage,
429 defects in the Tol-Pal system, periplasmic proteins implicated in linkages between inner
430 membrane, cell wall and outer membrane, severely impaired recovery of stationary-
431 phase cells. Stationary phase Δ*tolA* mutants exhibited blebbing and lysis upon
432 resuspension in fresh medium, a fate at least superficially similar to the demise of *mlaA**
433 mutants after an extended period in spent LB (7).
434
435 Together, these results suggest a model in which loss of connections between outer and
436 inner membrane synthesis contribute to shrinkage and that restoration of these
437 connections is critical to recovery. The strong bias toward sudden nutrient starvation-
438 induced shrinkage at the new pole (Fig. 2E) suggests that connections between the inner
439 and outer membrane develop subsequent to division, making the new pole more
440 vulnerable in this regard. The contribution of linkages between inner and outer
441 membrane to shrinkage and recovery is further supported by the importance of the Tol-
442 Pal system to efficient recovery from stationary phase (Fig. 6D). Previously implicated
443 in maintaining viability during division (34), Tol-Pal may preserve cell envelope
444 integrity in starved and stationary-phase cells by maintaining connections between the
445 inner and outer membranes as the inner membrane shrinks and expands. It remains
446 unclear whether loss of connections between the membranes directly causes water loss
447 from the cytoplasm and hence condensation. *E. coli* cells were previously shown to

448 shrink substantially after a week of starvation, although some of this shrinkage was due
449 to loss of cellular material into the extracellular milieu (38). Regardless, observations of
450 starvation-induced cytoplasm shrinkage in *K. pneumoniae* (Fig. 1C) and in *Vibrio cholerae*
451 (39) suggest that shrinkage may be widespread across Gram-negative bacteria.
452
453 Given the potentially generic nature of shrinkage across starvation conditions and the
454 independence of a variety of pathways, one possibility for the mechanism underlying
455 shrinkage is that the condensed cytoplasm is a passive result of the lack of metabolic
456 activity, akin to a previous hypothesis that the cytoplasm enters a "glassy" (less fluid)
457 state with dramatically slowed diffusion in energy-depleted conditions (20). However,
458 μNS diffusion was unaffected by starvation and shrinkage (Fig. S2A,B), suggesting that
459 energy depletion via starvation impacts cell physiology considerably differently than
460 energy depletion induced by an uncoupler. We previously discovered that diffusivity
461 does not change dramatically throughout density changes in fission yeast induced by
462 osmotic oscillations (16), suggesting that increased cytoplasmic density and/or reduced
463 metabolic capacity need not inhibit fluidization.
464
465 It is possible that shrinkage as cells lose water (Fig. 2F,G) is caused by a gradual
466 decrease in turgor pressure; a recent study found that immediately after nutrient
467 upshift volume increased more quickly than dry mass, similar to a hypoosmotic shock

468 (14). However, the mechanism by which cells would achieve such osmoregulation has
469 yet to be determined; an intriguing speculation motivated by the defects in Tol-Pal
470 mutants is that the cell wall produces compressive forces that exert osmotic-like effects.
471
472 The extent to which starvation and shrinking can be beneficial (or even tolerated) is
473 unclear. Is cytoplasmic densification an adaptive benefit or a passive response to
474 starvation? One possibility is that carbon depletion stimulates cells to shrink as a way to
475 increase the concentration of the metabolic intermediates and enzymes involved in
476 carbon metabolism, thereby driving reactions forward. This behavior would allow
477 bacteria to turn 'worthless' intermediates into useful products/energy. Such a
478 mechanism would be similar to how enzyme clustering accelerates the processing of
479 intermediates through metabolic channeling (40), and is consistent with the tight
480 coupling between shrinkage and growth rate as cells emerge from stationary phase (Fig.
481 5). Identification of a mutant that does not exhibit detachment would empower
482 metabolomics studies to test this hypothesis, but we have been unsuccessful in
483 identifying such a mutant using targeted approaches (Fig. S2). There is likely a
484 maximum interval of starvation that *E. coli* cells can generally withstand, as cell viability
485 eventually drops during development of the GASP phenotype (41). Protein degradation
486 may also eventually lead to cells not being able to sense or use nutrients to expand the
487 inner membrane back to the cell wall, particularly since translation-related proteins

488 experience the largest decrease during starvation detected here (Fig. 2H). In budding
489 yeast, macromolecular mobility is restricted by glucose starvation due to a reduction in
490 cell volume (42) and by chemical inhibition of glycolysis (43). In the future, it will be
491 interesting to determine the generality of this behavior across organisms; the presence
492 or absence of shrinkage may reflect different environmental pressures during
493 starvation. Understanding the response of bacterial cells to rapid removal of nutrients
494 may also indicate mechanisms for surviving stressful environments. Ultimately, the
495 discovery of novel starvation responses in bacteria may provide insights into the
496 dynamics of host-host transmission, particularly in pathogens, and reveal novel targets
497 such as Tol-Pal for disrupting starvation recovery.

498 **Author Contributions**

499 H.S., C.W., K.C.H., and P.L. conceived of and designed the research; H.S., C.W., J.K.,
500 P.D.O., S.C., M.S., J.M., C.G.G., and L.Z. performed the research; H.S., C.W., J.K.,
501 K.C.H., and P.A.L. analyzed the data; and H.S., C.W., F.C., P.L., and K.C.H. wrote the
502 paper. All authors reviewed the paper before submission.

503

504 **Acknowledgments**

505 The authors thank the Huang and Levin labs for helpful discussions, Sarah Anderson
506 for images of *Klebsiella pneumoniae,* and Christine Jacobs-Wagner for generously sharing
507 the μNS strain. Funding was provided by a Stanford Interdisciplinary Graduate
508 Fellowship, an Agilent Graduate Fellowship, and a James McDonnell Postdoctoral
509 Fellowship (to H.S.); a postdoctoral fellowship from the Swiss National Science
510 Foundation under Grant P400PB_180872 (to P.D.O.); a Stanford Graduate Fellowship
511 and National Science Foundation Graduate Research Fellowship (to S.C.); an Arnold O.
512 Beckman Postdoctoral Fellowship (to C.S.W.); the Washington University UStar and
513 SURF programs (to J.K.); NIH R01-GM056836 (to F. C.); NSF CAREER Award MCB-
514 1149328, and the Allen Discovery Center at Stanford on Systems Modeling of Infection
515 (to K.C.H); and NIH R35-GM127331 (to. P.A.L.). K.C.H. is a Chan Zuckerberg
516 Investigator.

517 **Methods**

518

519 ***Strains and growth media***

520 Cells were initially grown in lysogeny broth (LB) medium or AB+0.2% glucose at 37 °C
521 into log phase. Minimal growth medium made with AB (44) or M9 salts was used for all
522 starvation experiments. Antibiotics were used at the following concentrations:
523 ampicillin, 100 μg/mL; chloramphenicol, 30 μg/mL; rifampicin, 50 μg/mL; cerulenin, 100
524 μg/mL; A22, 2 μg/mL.

525

526 All knockouts were generated in *E. coli* MG1655 cells via transduction from the Keio
527 collection (45).

528

529 ***Starvation protocol***

530 Cells were first cultured in LB or M9+0.4% glucose and grown to an optical density at
531 600 nm of 0.1-0.2. Then, 0.8 mL of the culture were transferred to a 1-mL
532 microcentrifuge tube and spun at 8,500*g* for 1 min. The supernatant was immediately
533 removed and 1 mL of AB or M9 medium without carbon was added to the tube to wash
534 the cells. This washing procedure was repeated three times. The medium with the
535 resuspended pellet was placed in a test tube and shaken at 225 rpm at 37 °C for the
536 specified amount of time.

537

538 ***Single-cell imaging***

539 Agarose pads used for imaging were made by heating a solution containing 1% agarose
540 in the desired growth medium, and then allowing the solution to cool. 1-2 microliters of
541 solution containing starved cells were placed on the pads and allowed to air dry before
542 a coverslip was placed on the agarose pad.

543

544 Phase-contrast and fluorescence images were acquired with a Nikon Ti-E inverted
545 microscope (Nikon Instruments) using a 100X (NA 1.40) oil immersion objective and a
546 Neo 5.5 sCMOS camera (Andor Technology). The microscope was outfitted with an
547 active-control environmental chamber for temperature regulation (HaisonTech, Taipei,
548 Taiwan). Images were acquired using μManager v.1.4 (www.micro-manager.org) (46).

549

550 *K. pneumoniae* images were acquired on a Nikon Ti-E inverted microscope equipped
551 with a 100X Plan N (NA 1.25) objective (Nikon), SOLA SE Light Engine (Lumencor),
552 heated control chamber (OKO Labs), and ORCA-Flash4.0 sCMOS camera (Hamamatsu
553 Photonics). Fluorescence filter sets were purchased from Chroma Technology
554 Corporation. Nikon Elements software (Nikon Instruments) was used for image
555 acquisition.

556

557 ***Microfluidics***

558 Overnight cultures were diluted 100-fold into 1 mL of fresh LB and incubated for 2 h
559 with shaking at 37 °C, excepting experiments in minimal medium, for which overnight
560 cultures were diluted into M9+0.4% glucose and incubated for 4 h. Cells were imaged in
561 B04A microfluidic perfusion plates (CellASIC Corp.) and medium was exchanged using
562 the ONIX microfluidic platform (CellASIC Corp.). Plates were loaded with medium
563 pre-warmed to 37 °C. Cells were loaded into the plate, which was incubated at 37 °C,
564 without shaking, for 30 min before imaging.

565

566 ***Image analysis***

567 The MATLAB (MathWorks) image-processing code *Morphometrics* (47) was used to
568 segment cells and to identify cell outlines from phase-contrast microscopy images. A
569 local coordinate system was generated for each cell outline using a method adapted
570 from *MicrobeTracker* (48). Cell widths were calculated by averaging the distances
571 between contour points perpendicular to the cell midline, excluding contour points
572 within the poles and sites of septation. Cell length was calculated as the length of the
573 midline from pole to pole. See figure legends for the number of cells analyzed (n) and
574 error bar definitions.

575

576 ***Quantitative phase imaging***

577 Cells stained with WGA488 were loaded into the imaging chamber of an ONIX B04A
578 microfluidic chip (CellASIC). Before imaging, Koehler illumination was configured and
579 the peak illumination intensity with 10-ms exposure time was set to the middle of the
580 dynamic range of the Zyla sCMOS 4.2 camera (Andor). μManager v. 1.41 was used to
581 automate acquisition of brightfield *z*-stacks with a step size of 100 nm from ±1 μm
582 around the focal plane (total of 21 imaging planes). Fluorescence images were taken at
583 the focal plane to extract the cell contours. Similar measurements were performed in
584 medium supplemented with 100 mg/mL BSA to calibrate the phase shift equivalent to
585 100 mg/mL biomass.
586
587 For analysis, seven brightfield images at different focal planes (3 slices above and below
588 separated by 200 nm) were used to calculate the phase information using a custom
589 Matlab script implementing a previously published algorithm (17, 18). In brief, this
590 method relates the phase information of the cell to intensity changes along the *z*-
591 direction. Equidistant, out-of-focus images above and below the focal plane are used to
592 estimate intensity changes at various defocus distances. A phase-shift map is
593 reconstructed in a non-linear, iterative fashion to solve the transport-of-intensity
594 equation (17).
595

596 A Gaussian peak was fitted to the background of each image and then corrected to be at
597 zero phase shift using an image-wide subtraction of the mean of the peak. Cell contours
598 were segmented using *Morphometrics* v. 1.1 using the fluorescence channel (for
599 shrunken cells, the cell contour includes the region of the enlarged periplasm), and the
600 intensity of pixels inside each cell was extracted to calculate the dry mass density.
601

602 ***Proteome extraction***

603 Overnight cultures were diluted 1:200 into LB and grown into exponential phase at
604 37 °C. Before and after 4 h of starvation, ~10^9 cells were harvested and washed in cold
605 PBS, then flash-frozen in liquid nitrogen. Two biological replicate samples were
606 collected for each condition. All samples were then thawed and resuspended in 500 μL
607 lysis buffer (6 M urea, 50 mM Tris-base buffer pH 8.1, and 5% sodium dodecyl sulfate)
608 and subjected to 10 min of bead beating. After centrifugation at 10,000*g* for 3 min, the
609 supernatants were reduced with 10 μL of 500 mM dithiothreitol (Millipore Sigma) and
610 alkylated with iodoacetamide (Millipore Sigma). The peptides were washed, digested,
611 and eluted using S-trap tubes (Protifi) following the manufacturer's protocols, desalted
612 via C18 solid-phase extraction (Sep-Pak Waters), and dried via vacuum centrifugation.
613 Peptide concentration was quantified for normalization using a Nanodrop ND-1000.
614

615 **Mass spectrometry proteomic analyses**

616 Peptides were resuspended in 0.2% formic acid to a final concentration of 0.5 μg/μL.
617 Subsequently, 1 μL was loaded onto an in-house laser-pulled 100-μm inner diameter
618 nanospray column packed to ~22 cm with ReproSil-Pur C18-AQ 3.0 m resin (Dr. Maisch
619 GmbH). Peptides were separated via reverse-phase chromatography on a Dionex
620 Ultimate 3000 HPLC. Buffer A of the mobile phase contained 0.1% formic acid in HPLC-
621 grade water, and buffer B contained 0.1% formic acid in acetonitrile. The HPLC used a
622 two-step linear gradient with 4-25% buffer B for 135 min followed by 25-45% buffer B
623 for 15 min at 0.400 μL/min. Peptides were analyzed on a LTQ Orbitrap Elite mass
624 spectrometer (Thermo Fisher Scientific) in data-dependent mode, with full mass
625 spectrometry scans acquired in the Orbitrap mass analyzer with a resolution of 60,000
626 and *m*/*z* range of 340-1,600. The top 20 most-abundant ions with intensity threshold
627 above 500 counts and charge states 2 and above were selected for fragmentation using
628 collision-induced dissociation (CID) with an isolation window of 2 *m*/*z*, normalized
629 collision energy of 35%, activation Q of 0.25, and activation time of 5 ms. The CID
630 fragments were analyzed in the ion trap with rapid scan rate. Dynamic exclusion was
631 enabled with repeat count of 1 and exclusion duration of 20 s. The AGC target was set
632 to 1,000,000 and 50,000 for full FTMS scans and ITMSn scans, respectively. The
633 maximum injection times were set to 250 ms and 100 ms for full FTMS scans and ITMSn
634 scans, respectively.
635

636 **Peptide/protein database searching**

637 Mass spectra were searched using Proteome Discoverer 2.2.0.388 using the built-in
638 SEQUEST search algorithm. The Uniprot canonical *E. coli* FASTA database (4350 protein
639 sequences downloaded on 2/9/2020) was used in this search, along with a database
640 containing common preparatory contaminants. The precursor mass range was set to
641 350-3000 Da, the mass error tolerance was set to 10 ppm, and the fragment mass error
642 tolerance to 0.6 Da. Enzyme specificity was set to trypsin, carbamidomethylation of
643 cysteines (57.021) was set as variable modifications, and oxidation of methionines
644 (+15.995) and acetylation of protein N-terminus (+42.011) were considered as variable
645 modifications. Percolator was used to filter peptides and proteins to a false discovery
646 rate of 1%. Abundance quantification was based on precursor ion peak areas.

647

648 **μNS tracking**

649 Analyses were performed as previously described (20). Briefly, cell outlines were
650 extracted using *Morphometrics* (47) from phase contrast images. Local cell coordinates
651 were defined based on the mesh algorithm in *MicrobeTracker* (48), and particle motion
652 was quantified using these local coordinates along the long and short axes of the cell.
653 The fluorescent GFP-μNS particles appeared as diffraction-limited spots, and their
654 positions were determined relative to the cell coordinates by a Gaussian fit in two
655 dimensions.

656

657 **Statistical analyses**

658 Two-tailed Student's *t*-tests were used in Fig. 1E, 2B, and 3B,D,F. Fisher's exact tests

659 were used in Fig. 1G,H. All *p*-values and sample sizes *n* are included in the

660 corresponding figures and/or figure legends.

661 **Figure Legends**

662

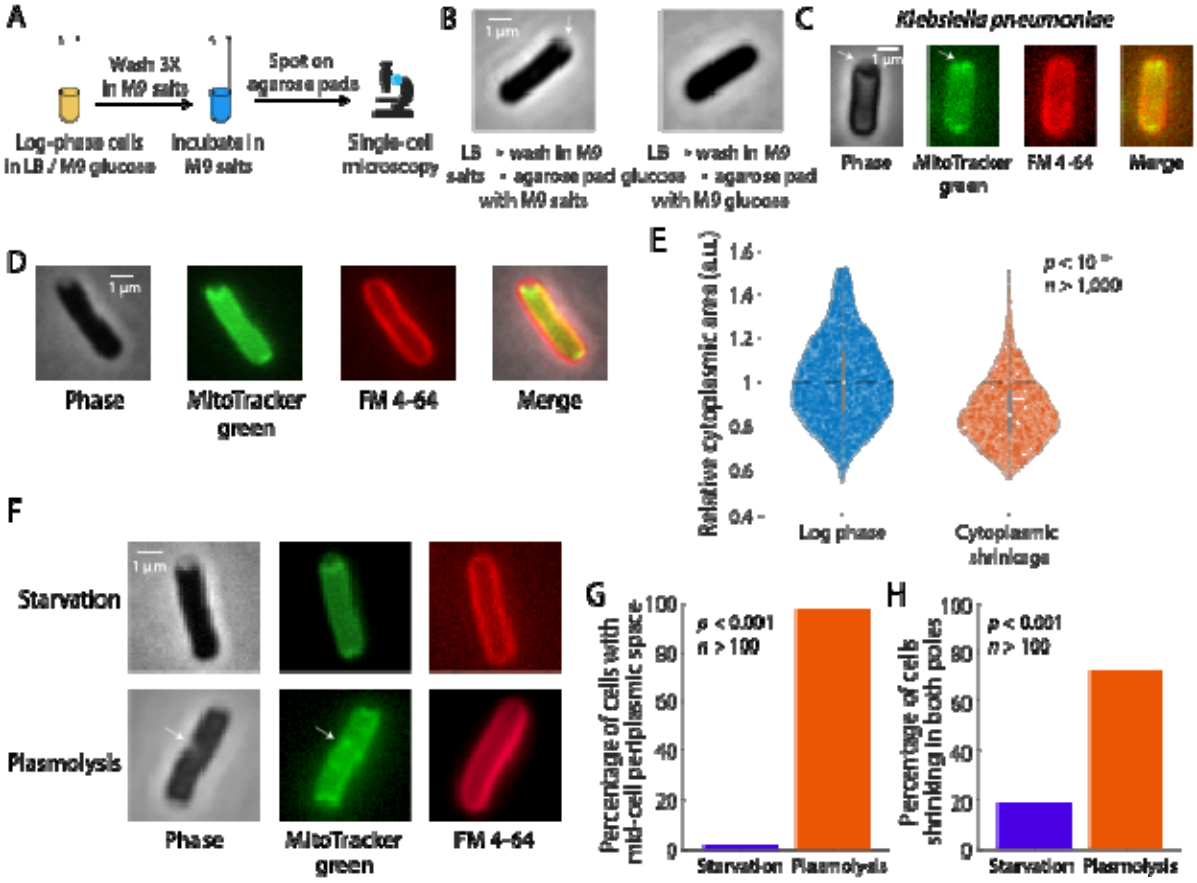

663

664 **Figure 1: Carbon starvation causes the *E. coli* cytoplasm to shrink in a manner distinct**

665 **from plasmolysis.**

666 A) Experimental setup for inducing cytoplasmic shrinkage. Log-phase cells were

667 pelleted and washed in M9 salts, then incubated in M9 salts without carbon

668 source. The resulting cells were placed onto agarose pads containing M9 salts

669 and imaged.

670 B) Left: log-phase cells grown in LB were washed in M9 salts three times and

671 immediately placed on an agarose pad. Shrinkage of the cytoplasm was observed
672 in most cells (white arrow). Right: washing in M9 glucose did not cause
673 shrinkage.
674 C) Shrinkage was also observed in *Klebsiella pneumoniae* cells after transitioning from
675 LB to M9. White arrows highlight the pole with shrinkage.
676 D) Staining of carbon-starved MG1655 cells revealed clear separation between the
677 outer membrane dye FM4-64 and the inner membrane dye MitoTracker at one
678 pole.
679 E) After 4 h of starvation, the relative cytoplasmic areas of starved cells as
680 quantified by segmenting the MitoTracker signal were ~17% smaller than those
681 of log-phase cells.
682 F) Representative *E. coli* MG1655 cells 4 h after rapid starvation induced by
683 transition from LB into M9 salts (top) or after a hyperosmotic shock with 3 M
684 sorbitol (bottom). After hyperosmotic shock, plasmolysis bays along the cell
685 body (arrows) were visible in phase-contrast and from MitoTracker staining, and
686 the cytoplasm was visibly smaller at both ends. By contrast, the cytoplasm of the
687 starved cell was shrunk only at one pole. FM4-64 stains the outer membrane,
688 which remained largely unaffected in both cases.
689 G, H) The percentage of cells that that exhibited mid-cell periplasmic spaces (G) or
690 shrinkage at both poles (H) was significantly higher for osmotic shock-induced

plasmolysis than for starvation (Fisher's exact test).

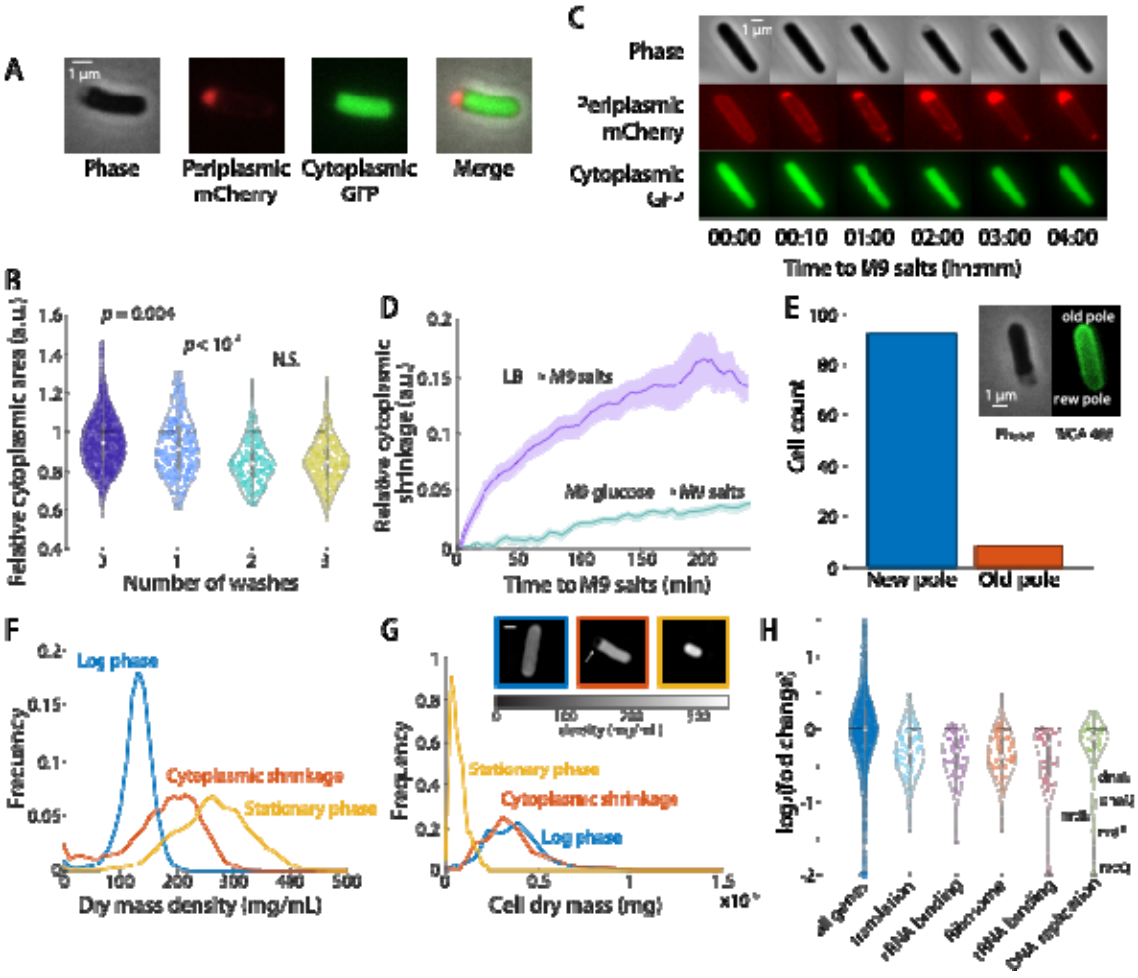

Figure 2: Cytoplasmic shrinkage is sensitive to the extent and duration of nutrient removal, and increases cell dry-mass density.

A) Representative images of phase-contrast, cytoplasmic GFP, and periplasmic mCherry images of KC1193 cells after transitioning from LB to M9 salts for 4 h. Shrinkage of the cytoplasm was evident by the bright periplasmic mCherry signal.

B) The relative cytoplasmic area of KC1193 cells (as measured by the GFP signal relative to the total cell area with GFP or mCherry signal) plateaued only after

701 multiple washes. $n > 100$ cells for each condition, and p-values were calculated
702 from two-tailed Student's t-tests.
703 C) After shifting from LB to M9 salts in a microfluidic chamber, the cytoplasmic
704 area of KC1193 cells continued to decrease for several hours.
705 D) The rate of shrinkage was faster in cells transitioned from LB to M9 salts
706 compared to transitioning from M9 glucose to M9 salts. Data points are mean ±
707 standard error of mean (sem) for $n>100$ cells in each condition.
708 E) Cytoplasmic shrinkage occurs predominantly at the new pole. After pulse-chase
709 labeling with Alexa488-WGA to label the cell periphery, the pole with separation
710 between the cytoplasm and cell wall was almost always at the unlabeled (new)
711 cell pole. Inset: a typical cell with shrinkage in the new (dark) pole.
712 F) Quantitative phase imaging demonstrated that starved cells have higher dry-
713 mass density than exponentially growing cells, yet the density is still lower
714 compared to stationary-phase cells ($n > 200$ cells for each condition).
715 G) The total dry mass of starved cells was similar to that of exponentially growing
716 cells. Inset: typical quantitative phase images for each condition, with the white
717 arrow highlighting the pole with shrinkage. Scale bar: 1 μm.
718 H) Proteomics measurements highlighted classes of proteins involved in translation
719 and DNA replication with significantly lower abundance in starved cells ($p <$
720 0.01, FDR < 0.05 with bootstrapping). Colored circles represent data from

721 individual proteins. White circles are mean values across all proteins in the class

722 and error bars are 1.5 times the interquartile range.

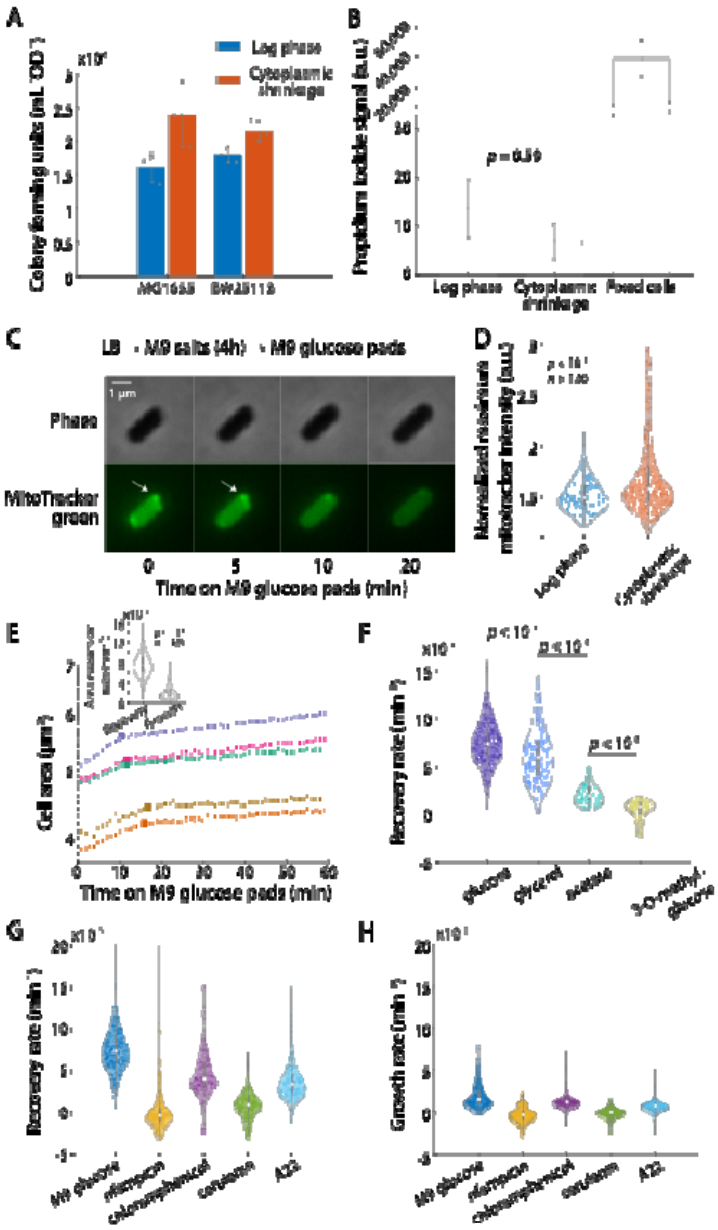

Figure 3: Recovery from starvation is slow and dependent on carbon-source quality.

A) Starvation did not reduce viable cell counts in either MG1655 and BW25113 cells, suggesting that all cells recovered from shrinkage and were able to regrow when exposed to fresh nutrient. Data points are mean ± standard deviation (S.D.) with *n*=3 replicates.

729 B) Propidium iodide staining was similarly low (n>100 cells, two-tailed Student's t-
730 test) in exponentially growing and starved cells as compared with cells killed
731 and fixed with ethanol.
732 C) Cells starved in M9 salts for 4 h were spotted onto an agarose pad with M9+0.4%
733 glucose and MitoTracker and monitored using time-lapse microscopy. The
734 cytoplasm began to re-expand almost immediately after cells were placed on the
735 agarose pad. Initially, cells exhibited bright MitoTracker foci, suggesting
736 membrane crumpling, and the foci appeared to dissolve as the cytoplasm re-
737 expanded.
738 D) MitoTracker signal is more uniformly distributed in exponentially growing cells
739 compared with starved cells (two-tailed Student's t-test), consistent with the
740 observation of inner membrane puncta in starved cells.
741 E) Typical single-cell traces of cytoplasmic area expansion after starved cells were
742 exposed to fresh nutrient again. The expansion rate was faster during the
743 recovery phase when inner membrane was shrunk away from the cell wall, but
744 slowed down after the inner membrane rejoined the cell wall. Individual round
745 dots are raw data, solid lines are best fits to exponential curves, and squares are
746 the best fit for the transition time from fast to slow expansion. Inset: area
747 expansion rate during recovery was faster than growth post-recovery (two-tailed
748 Student's t-test).

F) The recovery rate after starvation was dependent on the quality of carbon sources in the recovery media. Recovery was slower on carbon sources that support slower steady-state growth rates. Addition of the non-metabolizable glucose analog 3-O-methyl-glucose did not stimulate recovery. n>100 cells for each condition. p-values are from two-tailed Student's t-tests.

G,H) In the presence of different antibiotics, starved cells still recovered when exposed to fresh glucose. The recovery (G) and growth (H) rates after starvation were slower ($p<10^{-4}$ in all conditions, Student's t-test, n>100 cells) compared to the antibiotic-free control. In (D), (F), (G), and (H), colored circles represent data from individual cells. White circles are mean values across all cells in that condition and error bars are 1.5 times the interquartile range.

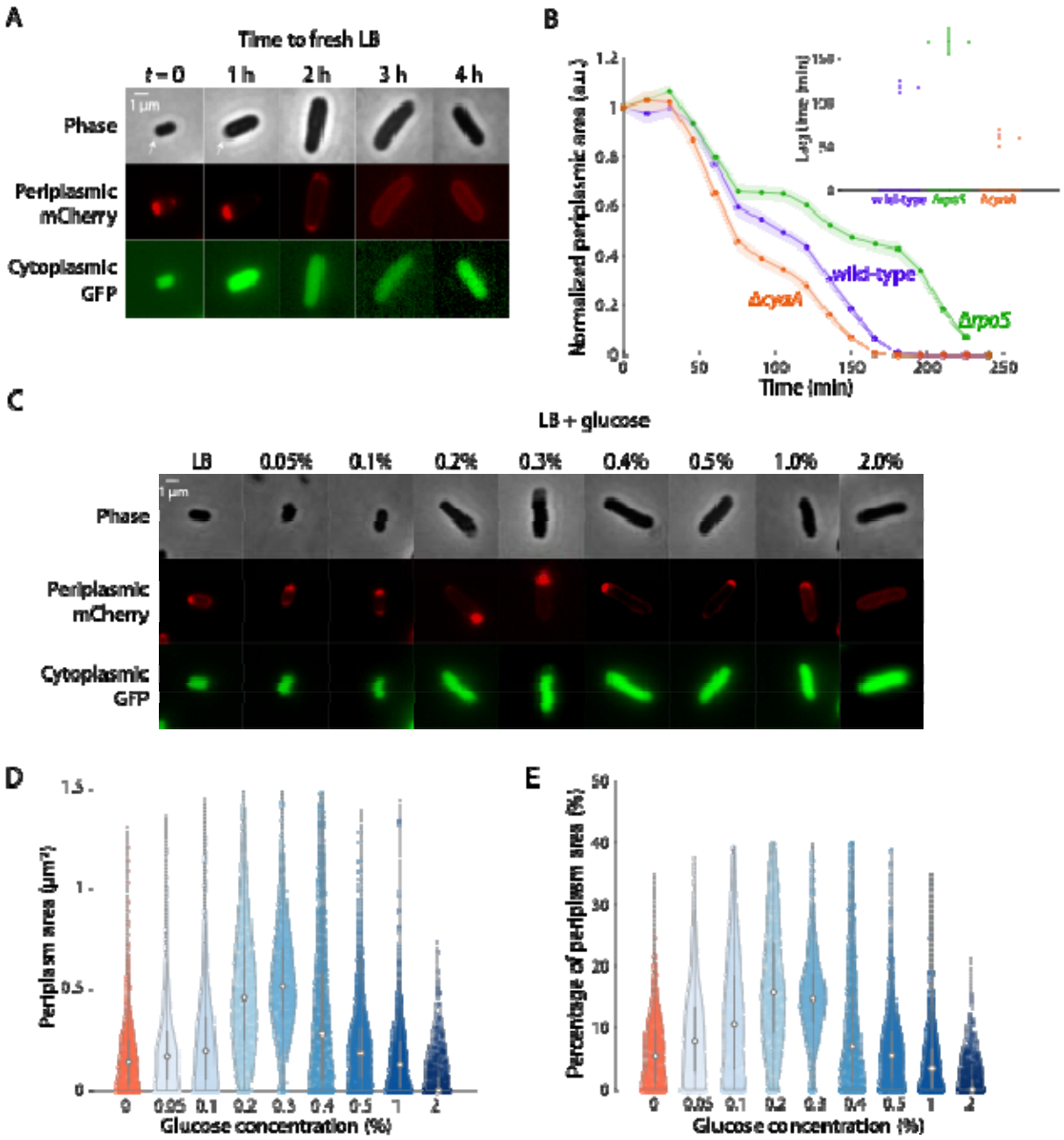

Figure 4: Shrinkage occurs during stationary phase and is exacerbated by intermediate levels of glucose.

A) Stationary-phase KC1193 cells exhibited a large periplasmic region that decreased in area over several hours after the cells were incubated in fresh LB.

765 B) The periplasmic area in Δ*rpoS* and Δ*cyaA* cells expressing periplasmic mCherry
766 resolved slower and faster, respectively, than in wild-type cells, consistent with
767 their differences in lag time (inset). Data points are mean ± sem with n>100 single
768 cells. Inset: lag times of each strain. Data points are mean ± S.D. with n=8
769 replicates.
770 C-E) Cells grown in LB+0.2-0.3% glucose have larger periplasmic spaces than cells
771 grown in LB or LB+2% glucose. Images in (C) are of KC1193 cells. The total
772 periplasmic area (D) and the periplasmic area normalized to total cell area (E) are
773 highest in LB+0.3% glucose. n>100 cells for each condition.

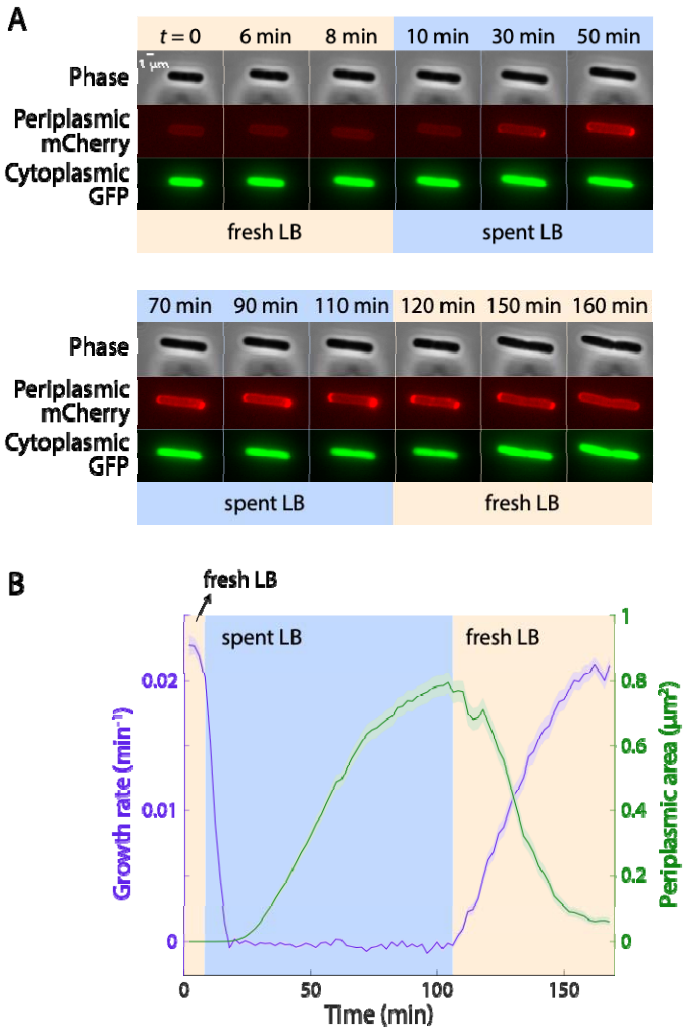

774

775 **Figure 5: Shrinkage initiates only once growth rate drops to zero, while gradual**

776 **growth resumption and resolution of periplasmic space occur simultaneously.**

777 A) Time-lapse images of KC1193 cells grown in fresh LB in a microfluidic flow cell

778 for 10 min, then switched to spent LB for 100 min, then switched back to fresh

779 LB. The osmolalities of the fresh and spent LB were equalized. The periplasmic

780 area has expanded after 20 min in spent LB, and gradually shrinks after the

781 resumption of growth in fresh LB.

782 B) Quantification of single-cell growth rate and periplasmic area revealed that
783 growth dropped to zero over ~10 min after switching to spent LB. The
784 periplasmic area only started to increase after the growth rate reached zero, and
785 increased steadily over the 100 min in spent LB. After the switch back to fresh
786 LB, growth rate immediately started to increase, gradually reaching pre-spent LB
787 levels after >60 min. The resolution of the periplasmic area was coincident with
788 the growth-rate increase. Data points are mean ± sem with n>150 cells.

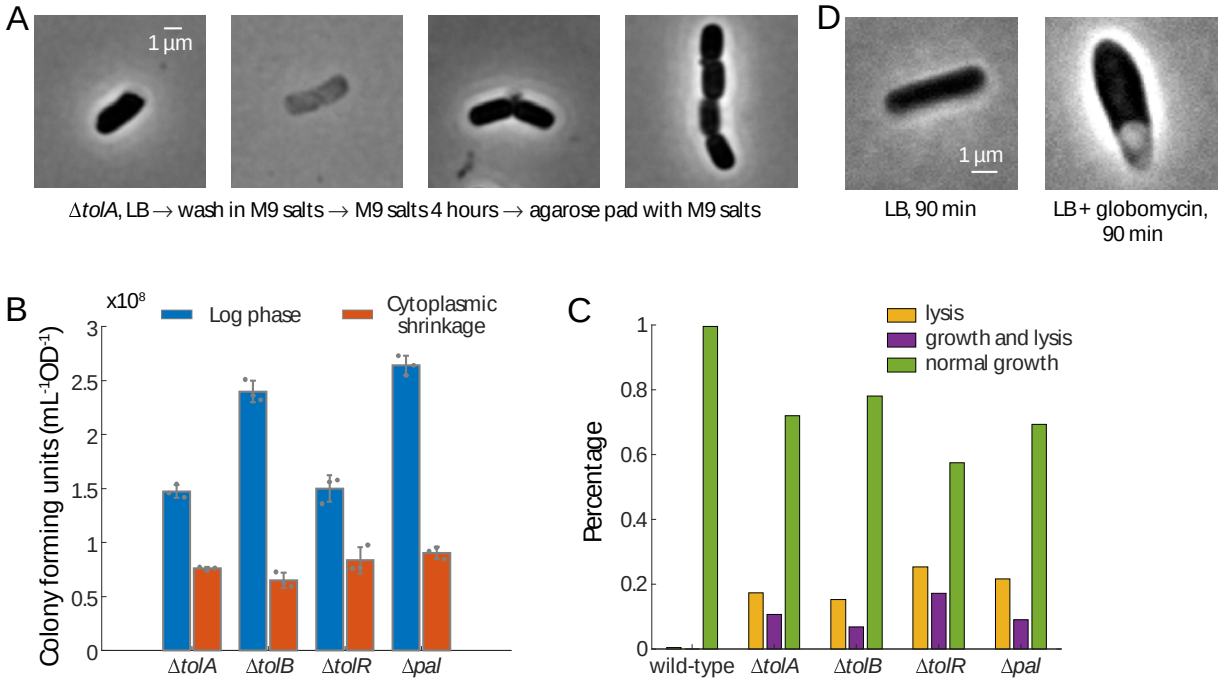

Figure 6: Shrinkage and recovery are dependent on a functional Tol-Pal system.

A) After 4 h of starvation in M9 salts, Δ*tolA* cells exhibited diverse phenotypes including shrinkage, lysis, blebbing and chaining.

B) The Tol-Pal pathway maintains viability during recovery from sudden starvation. All deletion mutants in the Tol-Pal pathway had 50-70% lower CFU yield compared to exponential phase, by contrast to the wild-type for which CFU levels were maintained (Fig. 3A). Data points are mean ± standard deviation (S.D.) with $n = 3$ replicates.

C) Quantification of the fraction of cells that outgrew from stationary phase. While virtually all wild-type cells resumed growth, 20-40% of Tol-Pal mutant cells

800 exhibited lysis within 3 h, suggesting that the Tol-Pal pathway is also critical

801 during recovery from normal stationary phase.

802 D) Treatment of exponentially growing cells with the lipoprotein signal peptidase II

803 inhibitor globomycin causes shrinkage. MG1655 cells were treated with 20

804 μg/mL globomycin for 90 min.

Supplemental Figures

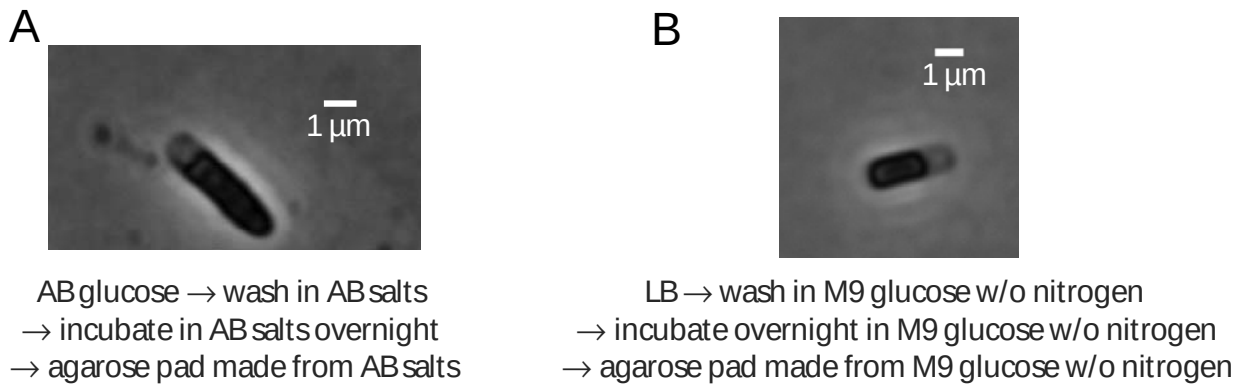

Figure S1: Shrinkage occurs during both carbon and nitrogen starvation.

A) Switching from AB glucose to AB salts led to similar shrinkage as switching from LB to M9 salts (Fig. 1B).

B) Nitrogen starvation also led to cytoplasmic shrinkage.

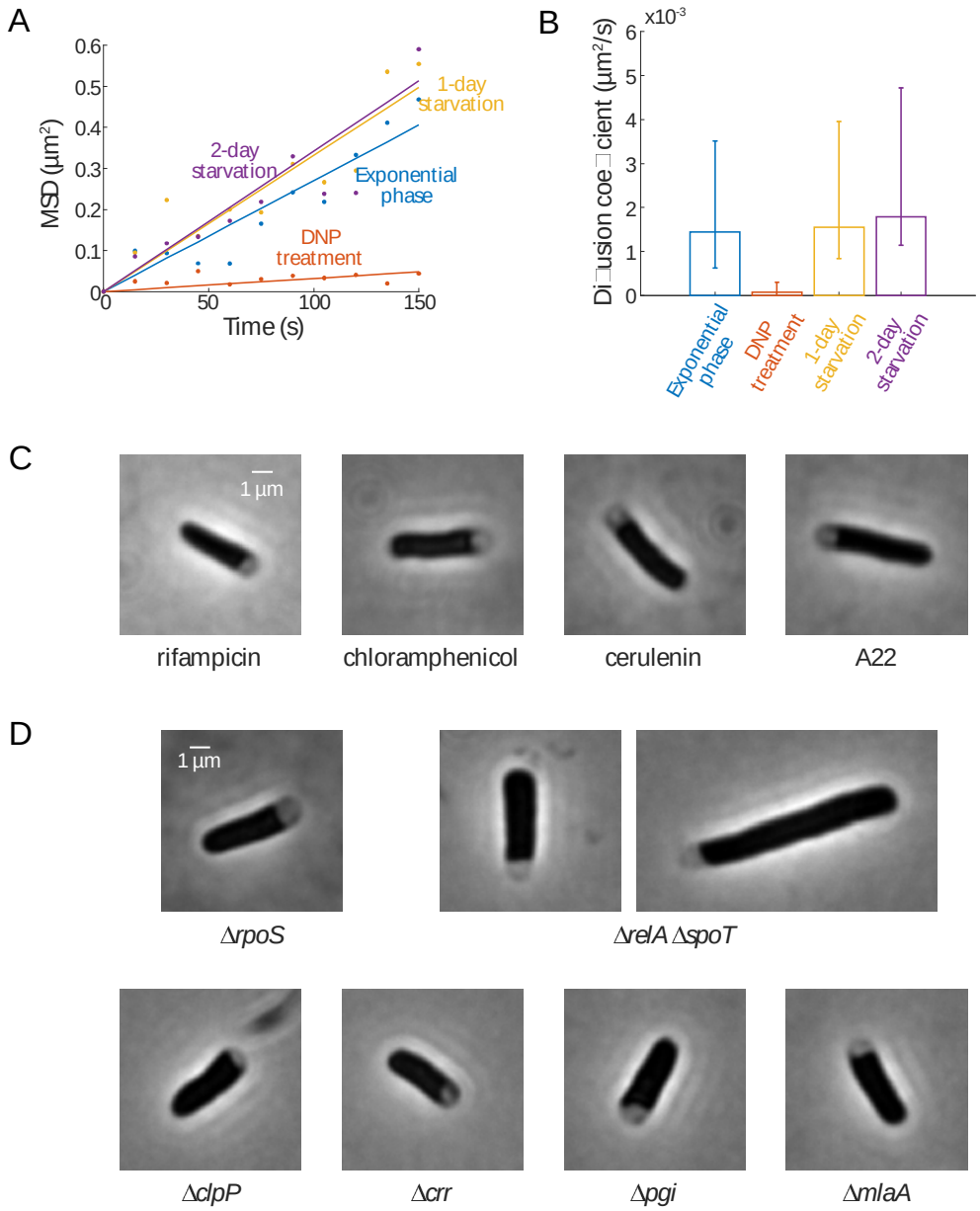

Figure S2: Shrinkage does not affect the diffusion of nanoparticles, and is not disrupted by a wide range of chemical or genetic perturbations.

A) Unlike treatment with DNP, carbon starvation did not slow down the diffusion constant D of μNS-GFP particles. Lines are linear fits of the raw data (dots), whose slopes are estimates of 4 times D. $n > 80$ tracks for each condition.

818 B) Carbon starvation did not change the effective diffusion coefficient of μNS-GFP

819 particles. Error bars are 95% confidence intervals.

820 C) Treatment at the time of transfer from LB to M9 salts with antibiotics that disrupt

821 transcription (rifampicin), translation (chloramphenicol), lipid synthesis

822 (cerulenin), or cell-wall synthesis (A22) did not affect shrinkage.

823 D) Shrinkage occurred in mutants that lack stringent-response regulators (Δ*rpoS*,

824 Δ*relA* Δ*spoT*, and Δ*clpP*), key enzymes in glucose processing (Δ*crr* and Δ*pgi*), or

825 components of outer-membrane transport (Δ*mlaA*).

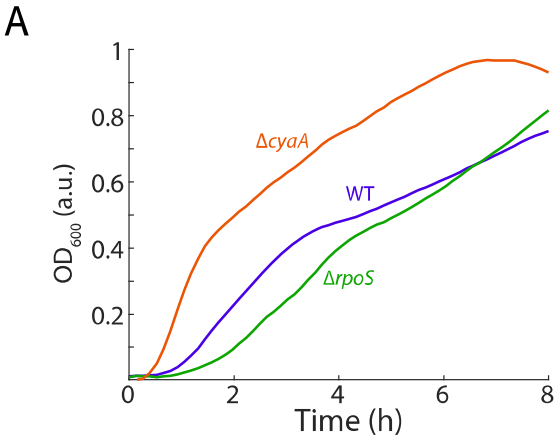

826

827 **Figure S3: Lag times in deletion mutants.**

828 Δ*cyaA* and Δ*rpoS* cells have shorter and longer lag times compared to wild-type cells,

829 which is connected to the different recovery dynamics in Fig. 4B.

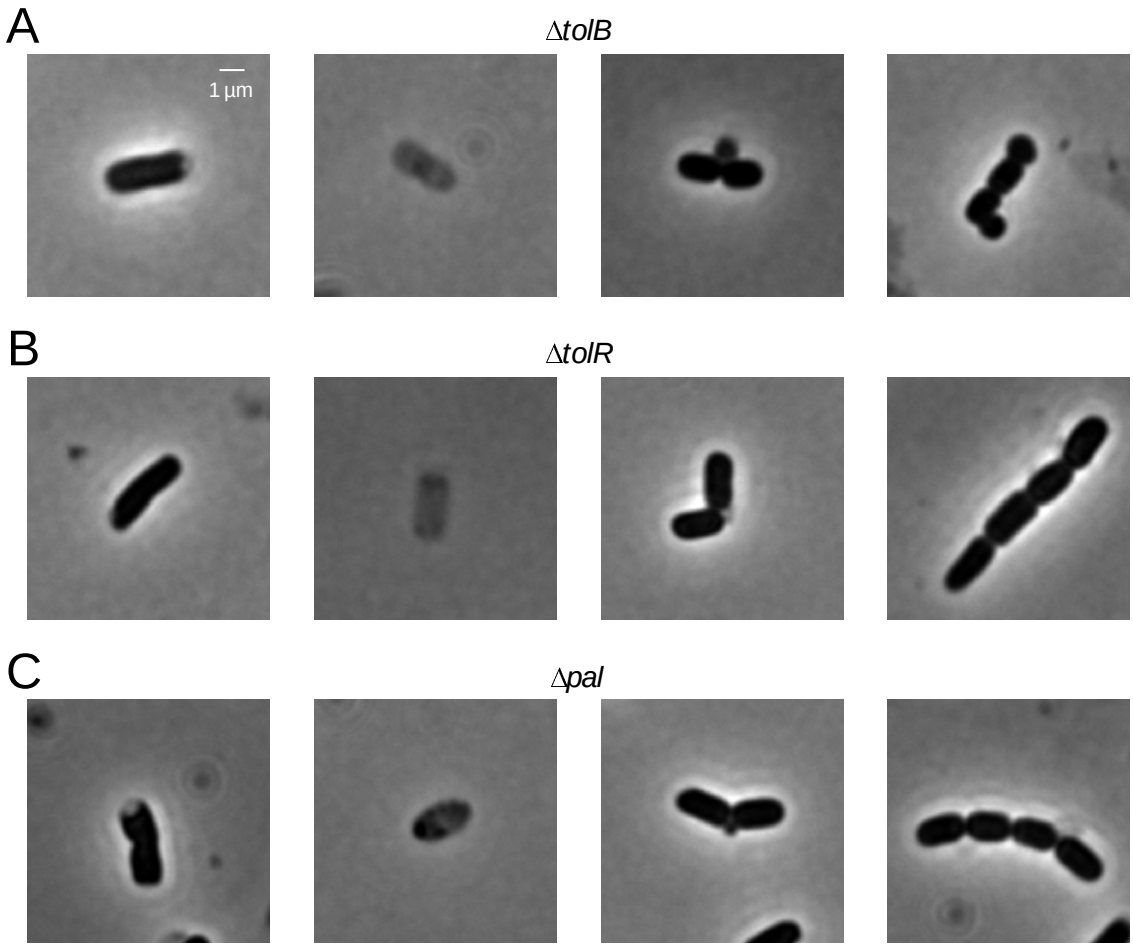

Figure S4: Deletion mutants in the Tol-Pal pathway leads to diverse phenotypes. After 4 h of starvation in M9 salts, Δ*tolB* (A), Δ*tolR* (B), and Δ*pal* (C) cells exhibited diverse phenotypes including shrinkage, lysis, blebbing and chaining, similar as Δ*tolA* (Fig. 6B).

836 **Supplemental Tables**

837

838 **Table S1: proteome measurements for log phase and starved cells.**

839 **References**

840

841 1. K. D. Young, The selective value of bacterial shape. *Microbiol Mol Biol Rev* **70**, 660-
842 703 (2006).
843 2. U. K. Sharma, D. Chatterji, Transcriptional switching in Escherichia coli during
844 stress and starvation by modulation of σ70 activity. *FEMS Microbiol. Rev.* **34**, 646-
845 657 (2010).
846 3. S. Iyer, D. Le, B. R. Park, M. Kim, Distinct mechanisms coordinate transcription
847 and translation under carbon and nitrogen starvation in Escherichia coli. *Nat.*
848 *Microbiol.* **3**, 741-748 (2018).
849 4. R. Kolter, D. A. Siegele, A. Tormo, The stationary phase of the bacterial life cycle.
850 *Annu Rev Microbiol* **47**, 855-874 (1993).
851 5. R. Lange, R. Hengge-Aronis, Identification of a central regulator of stationary-
852 phase gene expression in Escherichia coli. *Mol Microbiol* **5**, 49-59 (1991).
853 6. D. Weichart, R. Lange, N. Henneberg, R. Hengge-Aronis, Identification and
854 characterization of stationary phase inducible genes in Escherichia coli. *Mol*
855 *Microbiol* **10**, 407-420 (1993).
856 7. H. A. Sutterlin *et al.*, Disruption of lipid homeostasis in the Gram-negative cell
857 envelope activates a novel cell death pathway. *Proc Natl Acad Sci U S A* **113**,
858 E1565-1574 (2016).

859 8. G. Schreiber, E. Z. Ron, G. Glaser, ppGpp-mediated regulation of DNA
860 replication and cell division in Escherichia coli. *Curr Microbiol* **30**, 27-32 (1995).
861 9. S. Vadia *et al.*, Fatty Acid Availability Sets Cell Envelope Capacity and Dictates
862 Microbial Cell Size. *Curr Biol* **27**, 1757-1767 e1755 (2017).
863 10. E. Rojas, J. A. Theriot, K. C. Huang, Response of Escherichia coli growth rate to
864 osmotic shock. *Proc Natl Acad Sci U S A* **111**, 7807-7812 (2014).
865 11. W. W. Baldwin, R. Myer, T. Kung, E. Anderson, A. L. Koch, Growth and buoyant
866 density of Escherichia coli at very low osmolarities. *Journal of Bacteriology* **177**,
867 235-237 (1995).
868 12. C. N. Peterson, M. J. Mandel, T. J. Silhavy, Escherichia coli starvation diets:
869 essential nutrients weigh in distinctly. *J Bacteriol* **187**, 7549-7553 (2005).
870 13. T. S. Ursell *et al.*, Rod-like bacterial shape is maintained by feedback between cell
871 curvature and cytoskeletal localization. *Proc Natl Acad Sci U S A* **111**, E1025-1034
872 (2014).
873 14. E. R. Oldewurtel, Y. Kitahara, B. Cordier, G. Özbaykal, S. Van Teeffelen, Bacteria
874 control cell volume by coupling cell-surface expansion to dry-mass growth.
875 *BioRxiv*, 769786 (2019).
876 15. H. Shi, Y. Hu, K. C. Huang, Precise regulation of the relative rates of surface area
877 and volume synthesis in dynamic environments. *bioRxiv*, 806885 (2019).

878 16. B. D. Knapp *et al.*, Decoupling of Rates of Protein Synthesis from Cell Expansion
879 Leads to Supergrowth. *Cell Syst* **9**, 434-445 e436 (2019).
880 17. E. Bostan, E. Froustey, M. Nilchian, D. Sage, M. Unser, Variational Phase
881 Imaging Using the Transport-of-Intensity Equation. *IEEE Trans Image Process* **25**,
882 807-817 (2016).
883 18. P. D. Odermatt *et al.*, Variations of intracellular density during the cell cycle
884 arises from tip-growth regulation in fission yeast. *bioRxiv* (2020).
885 19. J. T. Mika, G. van den Bogaart, L. Veenhoff, V. Krasnikov, B. Poolman, Molecular
886 sieving properties of the cytoplasm of Escherichia coli and consequences of
887 osmotic stress. *Mol Microbiol* **77**, 200-207 (2010).
888 20. B. R. Parry *et al.*, The bacterial cytoplasm has glass-like properties and is
889 fluidized by metabolic activity. *Cell* **156**, 183-194 (2014).
890 21. K. Potrykus, M. Cashel, (p)ppGpp: still magical? *Annu Rev Microbiol* **62**, 35-51
891 (2008).
892 22. M. F. Traxler *et al.*, The global, ppGpp-mediated stringent response to amino acid
893 starvation in Escherichia coli. *Mol Microbiol* **68**, 1128-1148 (2008).
894 23. R. Hengge-Aronis, Survival of hunger and stress: the role of rpoS in early
895 stationary phase gene regulation in E. coli. *Cell* **72**, 165-168 (1993).
896 24. R. Hengge-Aronis, Recent insights into the general stress response regulatory
897 network in Escherichia coli. *J Mol Microbiol Biotechnol* **4**, 341-346 (2002).

898 25. B. S. Powell, D. L. Court, Control of ftsZ expression, cell division, and glutamine
899 metabolism in Luria-Bertani medium by the alarmone ppGpp in Escherichia coli.
900 *J Bacteriol* **180**, 1053-1062 (1998).
901 26. S. Rajagopal, N. Sudarsan, K. W. Nickerson, Sodium dodecyl sulfate
902 hypersensitivity of clpP and clpB mutants of Escherichia coli. *Appl Environ*
903 *Microbiol* **68**, 4117-4121 (2002).
904 27. D. Weichart, N. Querfurth, M. Dreger, R. Hengge-Aronis, Global role for ClpP-
905 containing proteases in stationary-phase adaptation of Escherichia coli. *J Bacteriol*
906 **185**, 115-125 (2003).
907 28. M. C. Jones-Mortimer, H. L. Kornberg, R. Maltby, P. D. Watts, Role of the crr-
908 gene in glucose uptake by Escherichia coli. *FEBS Lett* **74**, 17-19 (1977).
909 29. P. Charusanti *et al.*, Genetic basis of growth adaptation of Escherichia coli after
910 deletion of pgi, a major metabolic gene. *PLoS Genet* **6**, e1001186 (2010).
911 30. J. C. Malinverni, T. J. Silhavy, An ABC transport system that maintains lipid
912 asymmetry in the gram-negative outer membrane. *Proc Natl Acad Sci U S A* **106**,
913 8009-8014 (2009).
914 31. L. Boulos, M. Prevost, B. Barbeau, J. Coallier, R. Desjardins, LIVE/DEAD®
915 BacLight™: application of a new rapid staining method for direct enumeration of
916 viable and total bacteria in drinking water. *Journal of microbiological Methods* **37**,
917 77-86 (1999).

918 32. D. Schneider, E. Fuhrmann, I. Scholz, W. R. Hess, P. L. Graumann, Fluorescence
919 staining of live cyanobacterial cells suggest non-stringent chromosome
920 segregation and absence of a connection between cytoplasmic and thylakoid
921 membranes. *BMC Cell Biol* **8**, 39 (2007).
922 33. A. Pikis, S. Hess, I. Arnold, B. Erni, J. Thompson, Genetic requirements for
923 growth of Escherichia coli K12 on methyl-alpha-D-glucopyranoside and the five
924 alpha-D-glucosyl-D-fructose isomers of sucrose. *J Biol Chem* **281**, 17900-17908
925 (2006).
926 34. M. A. Gerding, Y. Ogata, N. D. Pecora, H. Niki, P. A. de Boer, The trans-envelope
927 Tol-Pal complex is part of the cell division machinery and required for proper
928 outer-membrane invagination during cell constriction in E. coli. *Mol Microbiol* **63**,
929 1008-1025 (2007).
930 35. N. Fognini-Lefebvre, J. C. Lazzaroni, R. Portalier, tolA, tolB and excC, three
931 cistrons involved in the control of pleiotropic release of periplasmic proteins by
932 Escherichia coli K12. *Mol Gen Genet* **209**, 391-395 (1987).
933 36. S. M. McLeod *et al.*, Small-molecule inhibitors of Gram-negative lipoprotein
934 trafficking discovered by phenotypic screening. *Journal of bacteriology* **197**, 1075-
935 1082 (2015).
936 37. V. W. Rowlett *et al.*, Impact of Membrane Phospholipid Alterations in Escherichia
937 coli on Cellular Function and Bacterial Stress Adaptation. *J Bacteriol* **199** (2017).

938 38. C. A. Reeve, P. S. Amy, A. Matin, Role of protein synthesis in the survival of
939 carbon-starved Escherichia coli K-12. *J Bacteriol* **160**, 1041-1046 (1984).
940 39. S. Brenzinger *et al.*, Structural and proteomic changes in viable but non-
941 culturable Vibrio cholerae. *Frontiers in microbiology* **10**, 793 (2019).
942 40. M. Castellana *et al.*, Enzyme clustering accelerates processing of intermediates
943 through metabolic channeling. *Nat Biotechnol* **32**, 1011-1018 (2014).
944 41. M. M. Zambrano, R. Kolter, GASPing for life in stationary phase. *Cell* **86**, 181-184
945 (1996).
946 42. R. P. Joyner *et al.*, A glucose-starvation response regulates the diffusion of
947 macromolecules. *Elife* **5** (2016).
948 43. M. C. Munder *et al.*, A pH-driven transition of the cytoplasm from a fluid- to a
949 solid-like state promotes entry into dormancy. *Elife* **5** (2016).
950 44. K. Makarova *et al.*, Comparative genomics of the lactic acid bacteria. *Proc Natl*
951 *Acad Sci U S A* **103**, 15611-15616 (2006).
952 45. T. Baba, H. Mori, The construction of systematic in-frame, single-gene knockout
953 mutant collection in Escherichia coli K-12. *Methods Mol Biol* **416**, 171-181 (2008).
954 46. A. Edelstein, N. Amodaj, K. Hoover, R. Vale, N. Stuurman, Computer control of
955 microscopes using microManager. *Curr Protoc Mol Biol* **Chapter 14**, Unit14 20
956 (2010).

957 47. T. Ursell *et al.*, Rapid, precise quantification of bacterial cellular dimensions
958 across a genomic-scale knockout library. *BMC Biol* **15**, 17 (2017).
959 48. O. Sliusarenko, J. Heinritz, T. Emonet, C. Jacobs-Wagner, High-throughput,
960 subpixel precision analysis of bacterial morphogenesis and intracellular spatio-
961 temporal dynamics. *Mol Microbiol* **80**, 612-627 (2011).
962

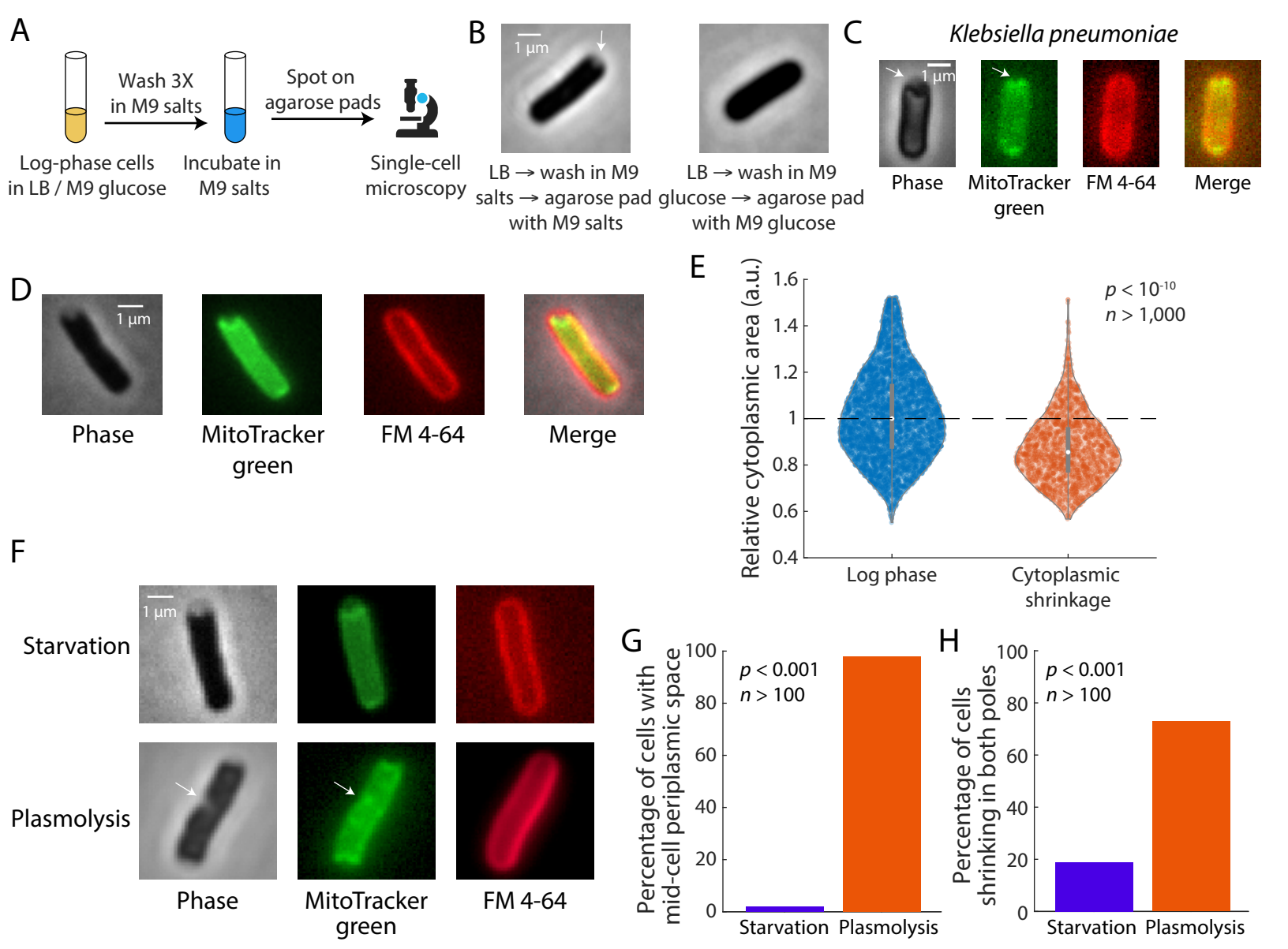
A
Wash 3X in M9 salts
Spot on agarose pads
Log-phase cells in LB / M9 glucose
Incubate in M9 salts
Single-cell microscopy
B
1 µm
LB → wash in M9 salts → agarose pad with M9 salts
LB → wash in M9 glucose → agarose pad with M9 glucose
C
Klebsiella pneumoniae
1 µm
Phase
MitoTracker green
FM 4-64
Merge
D
1 µm
Phase
MitoTracker green
FM 4-64
Merge
E
Relative cytoplasmic area (a.u.)
1.6
1.4
1.2
1
0.8
0.6
0.4
p < 10-10
n > 1,000
Log phase
Cytoplasmic shrinkage
F
Starvation
Plasmolysis
1 µm
Phase
MitoTracker green
FM 4-64
G
Percentage of cells with mid-cell periplasmic space
100
80
60
40
20
0
p < 0.001
n > 100
Starvation
Plasmolysis
H
Percentage of cells shrinking in both poles
100
80
60
40
20
0
p < 0.001
n > 100
Starvation
Plasmolysis

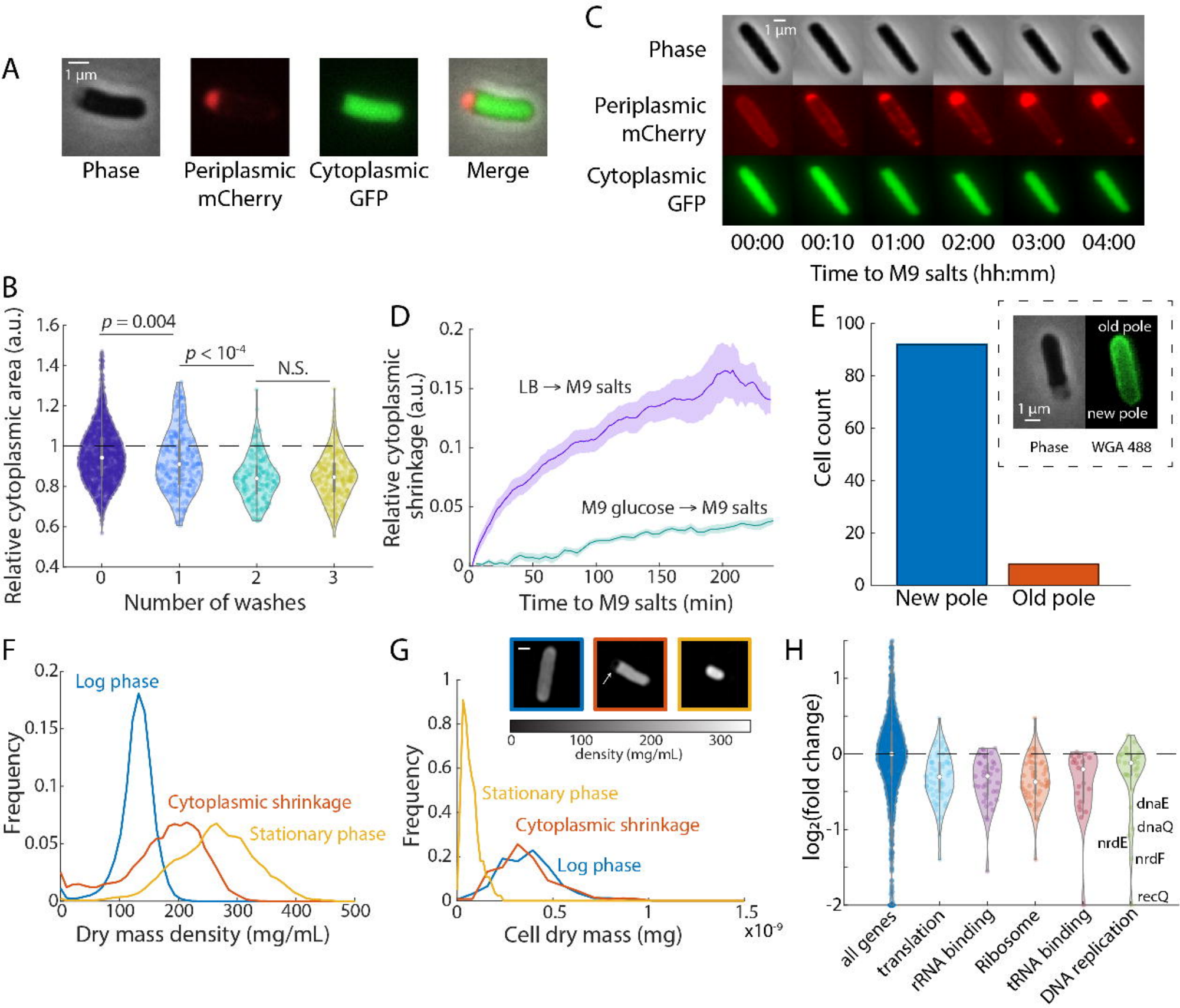
A
1 µm
Phase
Periplasmic mCherry
Cytoplasmic GFP
Merge
C
Phase
Periplasmic mCherry
Cytoplasmic GFP
1 µm
00:00
00:10
01:00
02:00
03:00
04:00
Time to M9 salts (hh:mm)
B
Relative cytoplasmic area (a.u.)
p = 0.004
p < 10-4
N.S.
Number of washes
D
Relative cytoplasmic shrinkage (a.u.)
LB → M9 salts
M9 glucose → M9 salts
Time to M9 salts (min)
E
Cell count
old pole
new pole
1 µm
Phase
WGA 488
New pole
Old pole
F
Frequency
Log phase
Cytoplasmic shrinkage
Stationary phase
Dry mass density (mg/mL)
G
Frequency
density (mg/mL)
Stationary phase
Cytoplasmic shrinkage
Log phase
Cell dry mass (mg)
x10-9
H
log2(fold change)
dnaE
dnaQ
nrdE
nrdF
recQ
all genes
translation
rRNA binding
Ribosome
tRNA binding
DNA replication

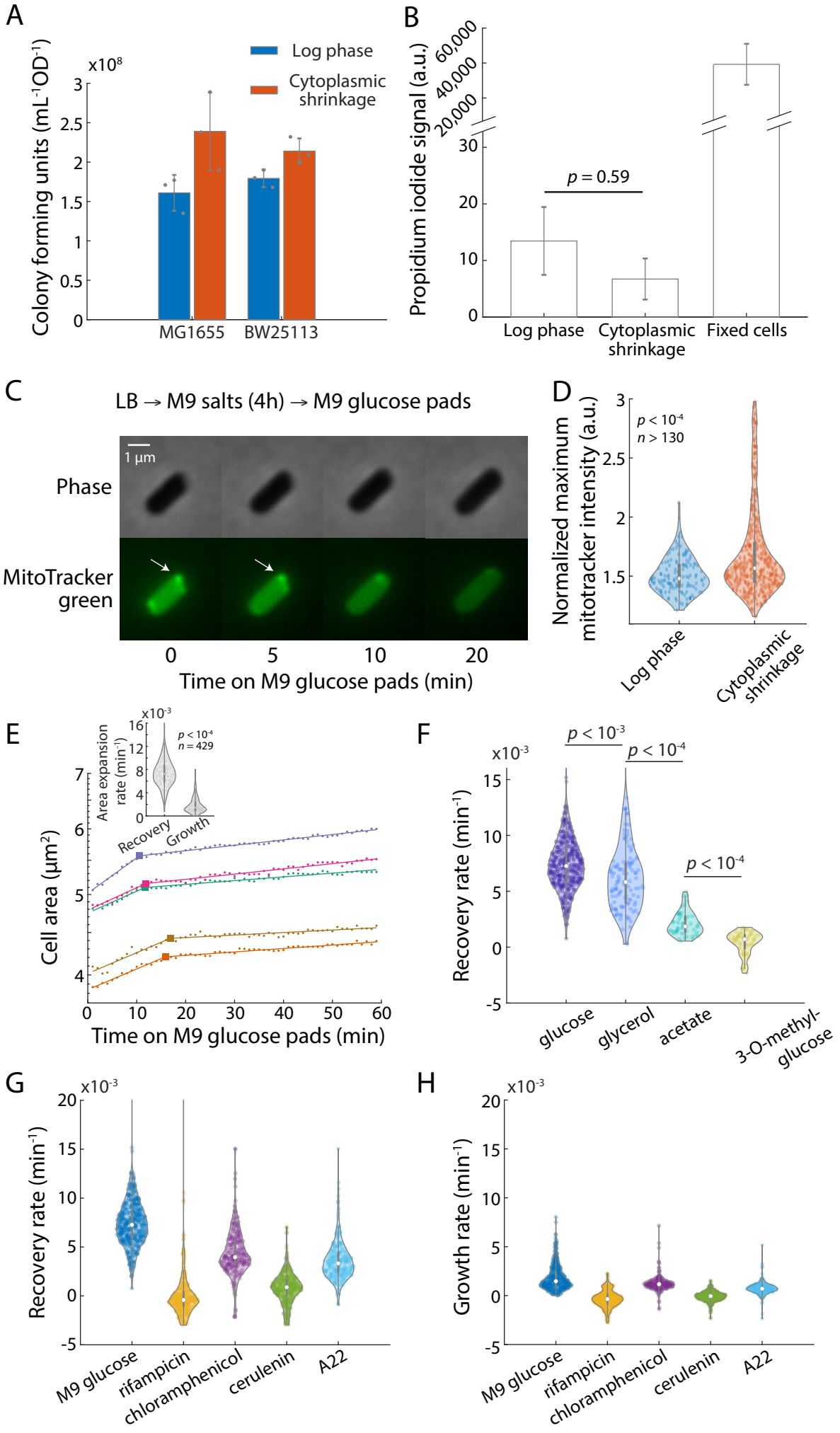
A
Colony forming units (mL-1OD-1)
x10^8
Log phase
Cytoplasmic shrinkage
MG1655
BW25113
B
Propidium iodide signal (a.u.)
p = 0.59
Log phase
Cytoplasmic shrinkage
Fixed cells
C
LB → M9 salts (4h) → M9 glucose pads
1 µm
Phase
MitoTracker green
Time on M9 glucose pads (min)
D
Normalized maximum mitotracker intensity (a.u.)
p < 10-4
n > 130
Log phase
Cytoplasmic shrinkage
E
Cell area (µm2)
Area expansion rate (min-1)
p < 10-4
n = 429
Recovery
Growth
Time on M9 glucose pads (min)
F
Recovery rate (min-1)
p < 10-3
p < 10-4
p < 10-4
glucose
glycerol
acetate
3-O-methyl-glucose
G
Recovery rate (min-1)
M9 glucose
rifampicin
chloramphenicol
cerulenin
A22
H
Growth rate (min-1)
M9 glucose
rifampicin
chloramphenicol
cerulenin
A22

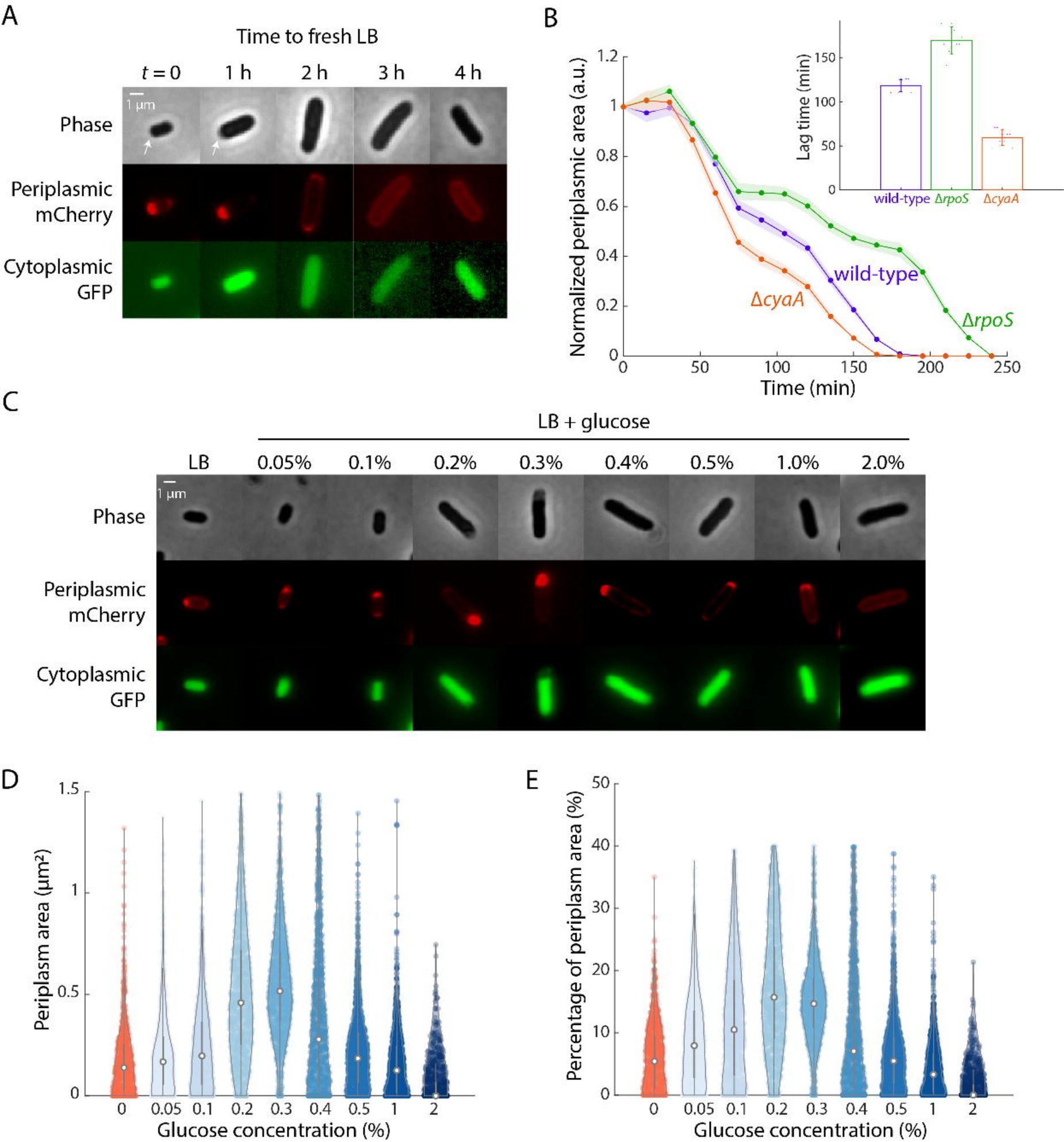
A
Time to fresh LB
t = 0
1 h
2 h
3 h
4 h
1 µm
Phase
Periplasmic mCherry
Cytoplasmic GFP
B
Normalized periplasmic area (a.u.)
Time (min)
Lag time (min)
wild-type
ΔrpoS
ΔcyaA
C
LB + glucose
LB
0.05%
0.1%
0.2%
0.3%
0.4%
0.5%
1.0%
2.0%
1 µm
Phase
Periplasmic mCherry
Cytoplasmic GFP
D
Periplasm area (µm²)
Glucose concentration (%)
E
Percentage of periplasm area (%)
Glucose concentration (%)

A

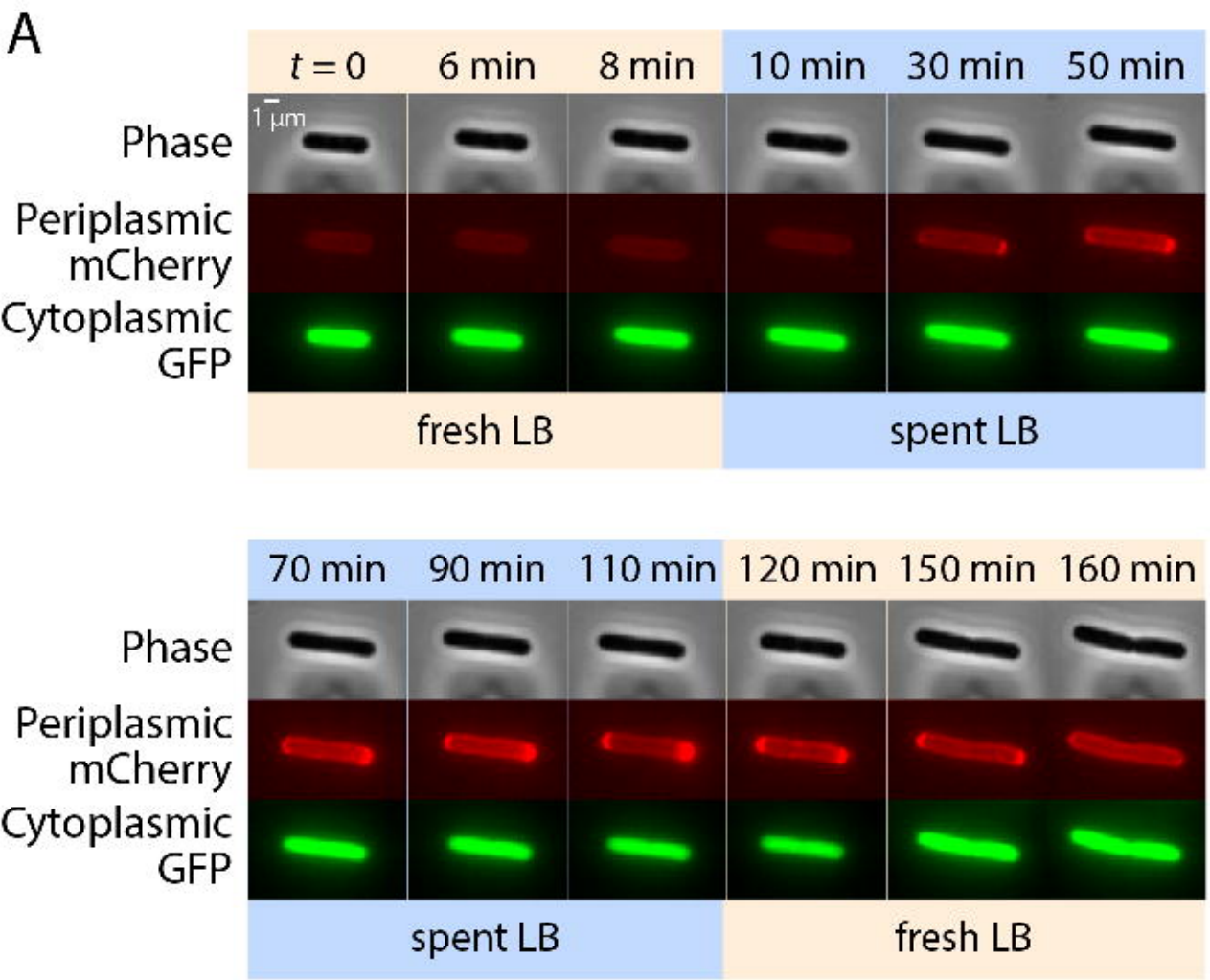
t = 0
6 min
8 min
10 min
30 min
50 min
1 µm
Phase
Periplasmic mCherry
Cytoplasmic GFP
fresh LB
spent LB
70 min
90 min
110 min
120 min
150 min
160 min
Phase
Periplasmic mCherry
Cytoplasmic GFP
spent LB
fresh LB

B

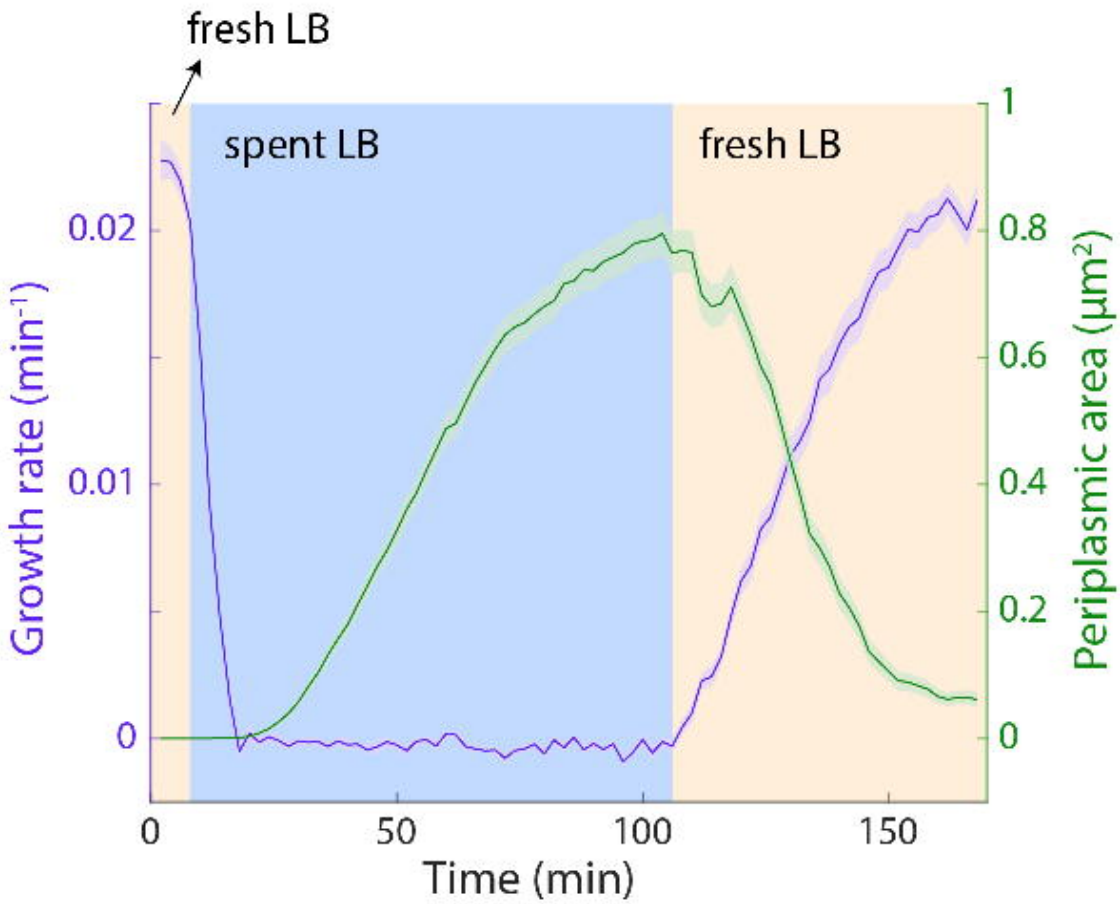
fresh LB
spent LB
fresh LB
Growth rate (min⁻¹)
0.02
0.01
0
Periplasmic area (µm²)
1
0.8
0.6
0.4
0.2
0
0
50
100
150
Time (min)

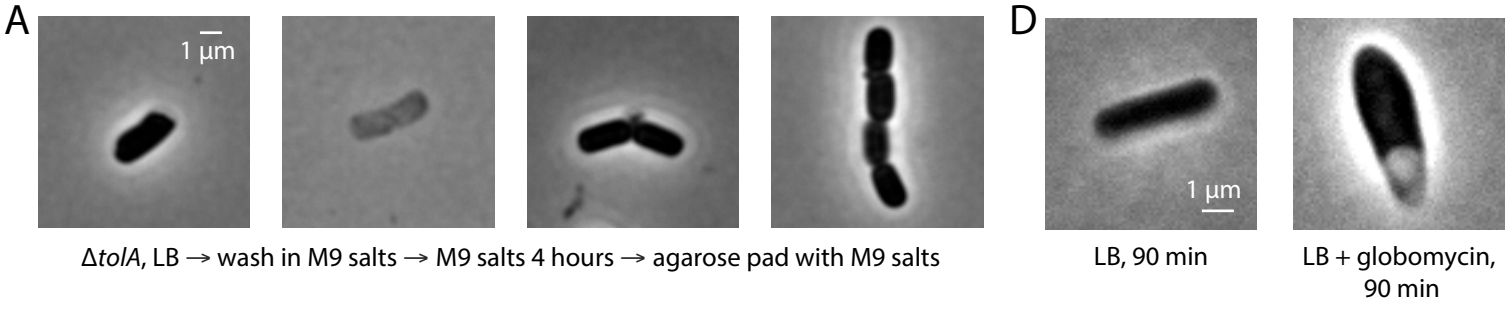
A
1 µm
ΔtolA, LB → wash in M9 salts → M9 salts 4 hours → agarose pad with M9 salts
D
1 µm
LB, 90 min
LB + globomycin, 90 min
B
x10^8
Log phase
Cytoplasmic shrinkage
Colony forming units (mL^-1OD^-1)
3
2.5
2
1.5
1
0.5
0
ΔtolA
ΔtolB
ΔtolR
Δpal
C
lysis
growth and lysis
normal growth
Percentage
1
0.8
0.6
0.4
0.2
0
wild-type
ΔtolA
ΔtolB
ΔtolR
Δpal